nature
biotechnology

Protection of tissue physicochemical properties using polyfunctional crosslinkers

Young-Gyun Park[1,2,12], Chang Ho Sohn[1,2,12], Ritchie Chen[1,2,12], Margaret McCue[1,2], Dae Hee Yun[1,2], Gabrielle T Drummond[1,2], Taeyun Ku[1,2], Nicholas B Evans[1,2], Hayeon Caitlyn Oak[3], Wendy Trieu[3], Heejin Choi[1,2], Xin Jin[1,4], Varoth Lilascharoen[5], Ji Wang[6], Matthias C Truttmann[7], Helena W Qi[8,9], Hidde L Ploegh[10], Todd R Golub[4], Shih-Chi Chen[6], Matthew P Frosch[11], Heather J Kulik[8], Byung Kook Lim[5] & Kwanghun Chung[1–4,8]

Understanding complex biological systems requires the system-wide characterization of both molecular and cellular features. Existing methods for spatial mapping of biomolecules in intact tissues suffer from information loss caused by degradation and tissue damage. We report a tissue transformation strategy named stabilization under harsh conditions via intramolecular epoxide linkages to prevent degradation (SHIELD), which uses a flexible polyepoxide to form controlled intra- and intermolecular crosslink with biomolecules. SHIELD preserves protein fluorescence and antigenicity, transcripts and tissue architecture under a wide range of harsh conditions. We applied SHIELD to interrogate system-level wiring, synaptic architecture, and molecular features of virally labeled neurons and their targets in mouse at single-cell resolution. We also demonstrated rapid three-dimensional phenotyping of core needle biopsies and human brain cells. SHIELD enables rapid, multiscale, integrated molecular phenotyping of both animal and clinical tissues.

Comprehensive understanding of biological systems requires the integration of molecular and structural information across multiple scales[1–6]. Existing approaches can profile multiple biomolecules, but only within a few layers of cells[7–9]. Techniques for processing intact tissue[10–17] enable organ-scale phenotyping, but can lead to information loss due to tissue damage and biomolecule degradation during processing, which may include digestion with proteases, delipidation, and exposure to high temperatures or dehydrating conditions. Such nonphysiological treatments can quench fluorescent proteins[13,18], degrade proteins[19], hydrolyze transcripts[20] and damage tissue architecture.

Various approaches have been proposed to preserve biomolecules against stressors. For example, changing biomolecule–solvent interactions by tuning solvent polarity or incorporating additives can preserve biomolecules in extreme conditions, but this requires high concentrations of additives that may interfere with tissue processing and probe–target interactions[21]. Covalent modification with chemical fixatives or encapsulation in hydrogels can secure biomolecules[22–24], but this is often accompanied by loss of biomolecule function and probe-binding affinity owing to structural and chemical damage[25,26]. Preserving protein fluorescence is particularly challenging because small alterations in tertiary structure can quench signal[27]. So far, no single method simultaneously preserves the full fluorescence of proteins, the reactivity of proteins with specific probes, integrity of transcripts, and tissue architecture across organs.

Here we introduce SHIELD (stabilization to harsh conditions via intramolecular epoxide linkages to prevent degradation), a versatile method that simultaneously preserves key molecular information— protein fluorescence, protein immunoreactivity and nucleic acids—in cleared intact tissues by using a polyfunctional, flexible epoxide. We attribute the cross-linker's protective mechanism to the formation of multiple flexible intramolecular bonds that enhance the stability of the protein's tertiary structure. When applied to tissue, SHIELD combined with SWITCH[14] enables uniform, organ-wide preservation of fluorescent protein activity, proteins, transcripts, and their probe-binding properties without loss of tissue architecture. SHIELD synergizes with several existing tissue processing technologies. For example, SHIELD combined with stochastic electrotransport[28] enables ultrafast 3D processing of whole needle biopsies and integrated phenotyping of parvalbumin (PV)-positive neurons in the globus pallidus externa (GPe) and their downstream targets.

[1]Institute for Medical Engineering and Science, Massachusetts Institute of Technology (MIT), Cambridge, Massachusetts, USA. [2]Picower Institute for Learning and Memory, MIT, Cambridge, Massachusetts, USA. [3]Department of Brain and Cognitive Sciences, MIT, Cambridge, Massachusetts, USA. [4]Broad Institute of Harvard University and MIT, Cambridge, Massachusetts, USA. [5]Neurobiology Section, Division of Biological Sciences, University of California, San Diego, La Jolla, California, USA. [6]Department of Mechanical and Automation Engineering, The Chinese University of Hong Kong, Shatin, Hong Kong. [7]Program in Cellular and Molecular Medicine, Boston Children's Hospital and Harvard Medical School, Boston, Massachusetts, USA. [8]Department of Chemical Engineering, MIT, Cambridge, Massachusetts, USA. [9]Department of Chemistry, MIT, Cambridge, Massachusetts, USA. [10]Boston Children's Hospital and Harvard Medical School, Boston, Massachusetts, USA. [11]C.S. Kubik Laboratory for Neuropathology, Massachusetts General Hospital and Harvard Medical School, Boston, Massachusetts, USA. [12]These authors contributed equally to this work. Correspondence should be addressed to K.C. (khchung@mit.edu).

RESULTS

Polyepoxide protects GFP fluorescence from stressors

We hypothesized that cross-linking surface-exposed protein residues with multiple flexible intramolecular bonds would provide structural reinforcement to enhance the stability of proteins. We screened polyepoxides because of their ability to form spontaneous cross-links with biomolecules under physiological conditions, backbone conformational flexibility and molecular diversity (**Fig. 1a** and **Supplementary Table 1**). Purified green fluorescent protein (GFP) was used as a model protein because loss of GFP fluorescence correlates directly with structural perturbations and loss of protein fluorescence affects many phenotyping technologies[29] (**Fig. 1b**).

We first performed molecular dynamics simulations of GFP to determine the side chain-to-side chain distance of solvent-exposed nucleophiles (lysine, histidine, cysteine and tyrosine) and found that the cross-linkable pairs spanned distances with increasing frequency above 10 Å (**Fig. 1c**). Cross-linkers thus should ideally possess multiple reactive groups that bridge side chain pairs to maximize the chance of forming intramolecular bonds. Among the lowest energy state conformers calculated for a library of epoxides (**Fig. 1a** and **Supplementary Table 1**), we found that the polyepoxy compound polyglycerol-3-polyglycidyl ether (P3PE) had the highest count and broadest distribution of epoxide functional groups complementing the pairwise side chain distances of GFP (**Fig. 1d**–**h**).

We next reacted GFP with P3PE and other epoxide cross-linkers to investigate their protective properties. Mass spectrometry measured fewer than 14 P3PE molecules attached per GFP, compared to the 20 available reactive groups that reacted with monomeric glycidyl methyl ether, which is indicative of multipoint intraprotein cross-linking (**Supplementary Fig. 1**). When we measured GFP fluorescence after exposure to denaturing conditions at 90 °C for 10 min or 70% methanol for 1 h, we found that fluorescence was best retained in both conditions by polyepoxy with three or more functional groups, with P3PE exhibiting among the best performance overall (**Fig. 1i**). Under all conditions tested, P3PE outperformed commonly used protein stabilizers (for example, xylitol)[30] (**Fig. 1i**).

To understand the protective mechanism of P3PE intramolecular cross-linking, we characterized the physicochemical properties of the P3PE–GFP conjugate using differential scanning calorimetry, circular dichroism and fluorescence spectroscopy. Differential scanning calorimetry showed that GFP cross-linked with dipropylene glycol diglycidyl ether or P3PE exhibited observable transitional enthalpy and an increased melting temperature (from 84 °C to 87 °C and 95 °C, respectively), whereas extensive aldehyde fixation (12 h at 37 °C) eliminated GFP's ability to undergo thermal denaturation[31] (**Fig. 1j**). The presence of denaturation enthalpy indicates that the flexible polyglycerol backbone of the polyepoxy accommodates thermal fluctuations. This flexibility was further evident in acid denaturation–renaturation experiments[32], in which P3PE partially preserved GFP's ability to refold but did not do so when GFP was reacted with glutaraldehyde (GA) and paraformaldehyde (PFA) (**Fig. 1k**). The rigid nature of GA and PFA fixation compromises GFP structure, as seen from the disruption of the beta sheet circular dichroism spectra in favor of random coils[33], which reduces fluorescence intensity (**Fig. 1l,m**). In contrast, the P3PE-GFP conjugate retained both its native protein conformation and fluorescent signal (**Fig. 1l,m**).

SHIELD protects fluorescent proteins without tissue autofluorescence increase

Consistent with our findings with purified GFP, tissue epoxidation can preserve fluorescent protein activity in tissue under harsh treatments. After heat exposure at 70 °C for 24 h, tissue reacted with P3PE retained GFP signal in Thy1::EGFP M-line brain slices, but PFA control or GA tissues did not (**Fig. 2a**). Of the polyepoxides tested, P3PE preserved signal best, and this protective effect extended to other fluorescent proteins (**Fig. 2b**–**d**). Moreover, P3PE-treated tissue retained GFP signal 50–400% more effectively than PFA-fixed tissue following exposure to detergents or organic solvents used in other tissue clearing methods (**Fig. 2e**). We termed the combination of tissue epoxidation with polyepoxide and subsequent delipidation SHIELD. We anticipate that SHIELD's ability to maximally preserve fluorescent protein signal can complement existing tissue-phenotyping methods requiring dehydration with alcohols, delipidation with organic solvents or detergents, or hydration with urea[18,34].

SHIELD tissue also exhibited inherently low tissue autofluorescence, in contrast to that treated with GA[35], which increases background autofluorescence and complicates imaging of structures with low signals (**Fig. 2a,f**)[14,36]. For example, imaging of neurons expressing mOrange in neurites and GFP in synaptic clusters suffered from a poor signal-to-noise ratio (SNR) in GA-fixed tissue (**Fig. 2f,g**). By contrast, tissues epoxidated with P3PE under the same condition (37 °C, 6 h) exhibited low background autofluorescence across a wide spectral range (**Fig. 2h**), making it possible to image both individual neurites and their associated synaptic clusters with excellent SNR (**Fig. 2f,g**).

SHIELD preserves organ-wide tissue physicochemical properties

We next determined whether SHIELD preserves endogenous proteins and their immunoreactivity. Of the 53 antibodies tested, all antibodies that were compatible with PFA-fixed control tissue were found to be compatible with SHIELD (**Supplementary Fig. 2** and **Supplementary Table 2**). Antibodies that poorly stained GA-treated tissue yielded better signal in SHIELD tissue, suggesting that epitopes affected by GA fixation were not perturbed by SHIELD (**Fig. 2i,j** and **Supplementary Fig. 2**). SHIELD's ability to cross-link tissue into a durable protein network allowed us to perform multiple rounds of immunostaining while retaining fluorescent protein signal (**Fig. 2k,l** and **Supplementary Fig. 2**).

We further investigated whether SHIELD preserves transcripts in cleared organ-scale tissue. We confirmed the formation of covalent bonds between epoxides and nucleic acids using mass spectrometry (**Supplementary Fig. 1**)[37]. To quantify the degree of transcript retention, we performed fluorescence *in situ* hybridization (FISH) on the poly(A) tail of mRNA using a 50-nt oligodeoxythymine ($(dT)_{50}$) labeled with Cy3 (**Fig. 2m,n**). The FISH signal in SHIELD tissue was higher than that in cleared PFA tissue and comparable to the signal obtained by 1-ethyl-3-3-dimethyl-aminopropyl carbodiimide (EDC) chemistry[12,38] (**Fig. 2m,n**), while maintaining higher fluorescent protein signal compared to EDC-CLARITY (**Supplementary Fig. 3**). We were able to detect various mRNAs, including cell-type and neural activity markers, in SHIELD tissues (**Fig. 2o,p** and **Supplementary Fig. 3**).

SHIELD transforms entire organs into mechanically robust and transparent substrates while uniformly preserving fluorescent protein signals, protein antigenicity, transcripts and tissue architecture (**Figs. 2q** and **3** and **Supplementary Figs. 4** and **5**). We previously showed that a uniform and transparent tissue matrix can be obtained by controlling the kinetics of GA fixation using SWITCH (system-wide control of interaction time and kinetics of chemicals)[14]. In this method, we homogeneously dispersed GA in tissue by suppressing reactivity at pH 3 before initiating sample-wide cross-linking by shifting
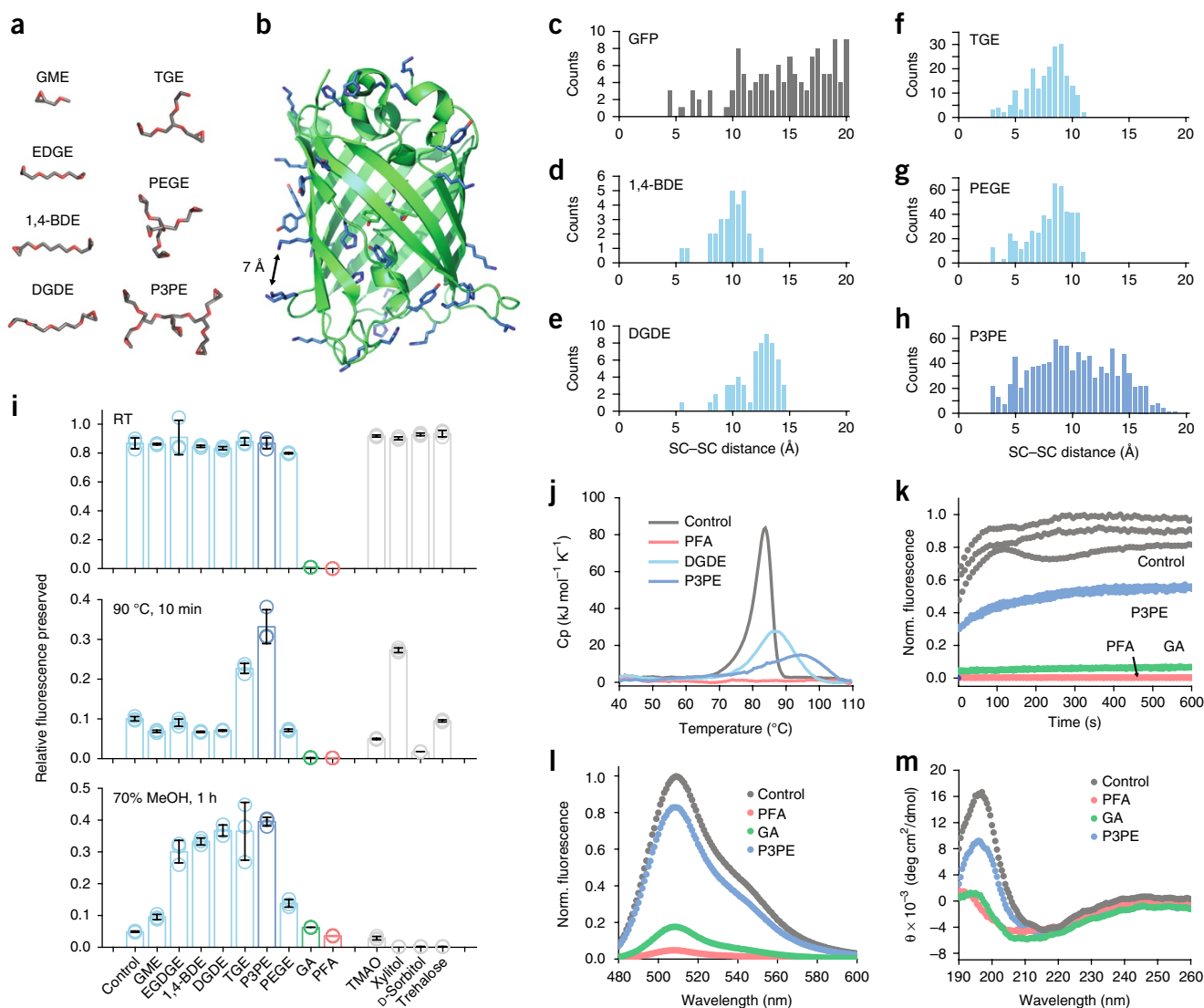
Figure 1 Protection of GFP activity with polyepoxide cross-linkers. (**a**) Representative lowest-energy conformers of epoxide molecules, drawn to the same scale as **b**. (**b**) GFP structure, with epoxide-reactive residues labeled in blue. The black arrow indicates a 7-Å distance between side chains. (**c**) Frequency count calculated for solvent-exposed GFP side chains (SC) as a function of their pairwise distances. (**d**–**h**) Frequency count of the average distance between epoxide groups, determined from the lowest-energy epoxide conformers. (**i**) Degree of GFP fluorescence preserved after reaction with cross-linkers (top) followed by exposure to 90 °C for 10 min (middle) or 70% methanol incubation for 1 h (bottom). $N = 3$ independent experiments. Mean ± s.e.m. (**j**) Differential scanning calorimetry plot of heat capacity as a function of the temperature of cross-linked GFP. (**k**) Plot of the fluorescence of cross-linked GFP recovered over time after renaturation from acid denaturation. (**l**) Fluorescence spectra of cross-linked GFP. (**m**) Circular dichroism spectra of cross-linked GFP. GME, glycidyl methyl ether; EGDGE, ethylene glycol diglycidyl ether; 1,4-BDE, 1,4-butanediol diglycidyl ether; DGDE, dipropylene glycol diglycidyl ether; TGE, glycerol triglycidyl ether; PEGE, pentaerythritol polyglycidyl ether; P3PE, polyglycerol 3-polyglycidyl ether; PFA, paraformaldehyde; GA, glutaraldehyde; TMAO, trimethylamine *N*-oxide.

to a neutral pH. However, the low pH of the GA SWITCH-off buffer can denature fluorescent proteins and hydrolyze transcripts, and GA generates autofluorescent byproducts[32,36] (**Fig. 2f,g**). In contrast, we found that the reactivity of the polyepoxide can be controlled at more physiological conditions, where reactivity with primary amines was suppressed at 4 °C, pH 7.4, and increased by tenfold at 37 °C, pH 10 (**Supplementary Fig. 5**). This SWITCH-mediated SHIELD reaction enabled preservation of transcripts in an intact organ-scale tissue cleared by stochastic electrotransport (**Fig. 2q** and **Supplementary Video 1**).

SWITCH-mediated SHIELD also preserves organ-scale tissue architecture. Delipidation of mouse brains can collapse lipid-rich

structures, which can deform connected regions and overall tissue structure (**Fig. 3a–d** and **Supplementary Fig. 4**). In particular, PFA-fixed tissues and polyacrylamide–tissue hybrids with a low degree of cross-linking or gel density can deteriorate under delabeling condition (70 °C for 2 h, 300 mM SDS) (**Fig. 3a,b** and **Supplementary Fig. 4**). Such widespread structural distortion can cause systematic errors in downstream image analysis and data interpretation. By contrast, SHIELD tissues exhibited no detectable distortion after delipidation and further destaining treatment (**Fig. 3a,b,d** and **Supplementary Fig. 4**). 3D imaging of a SHIELD brain hemisphere showed excellent brain-wide preservation of GFP signal and tissue architecture (**Supplementary Video 2**). This minimal tissue distortion

enabled automated atlas alignment and region segmentation (**Fig. 3g**). SHIELD samples are rigid and can be handled repeatedly without structural damage (**Fig. 3e,f**). Compared to existing methods, the ability to lock both transcripts and proteins within transparent organs while maximally preserving endogenous fluorescence and tissue architecture is a signature advantage of SHIELD.
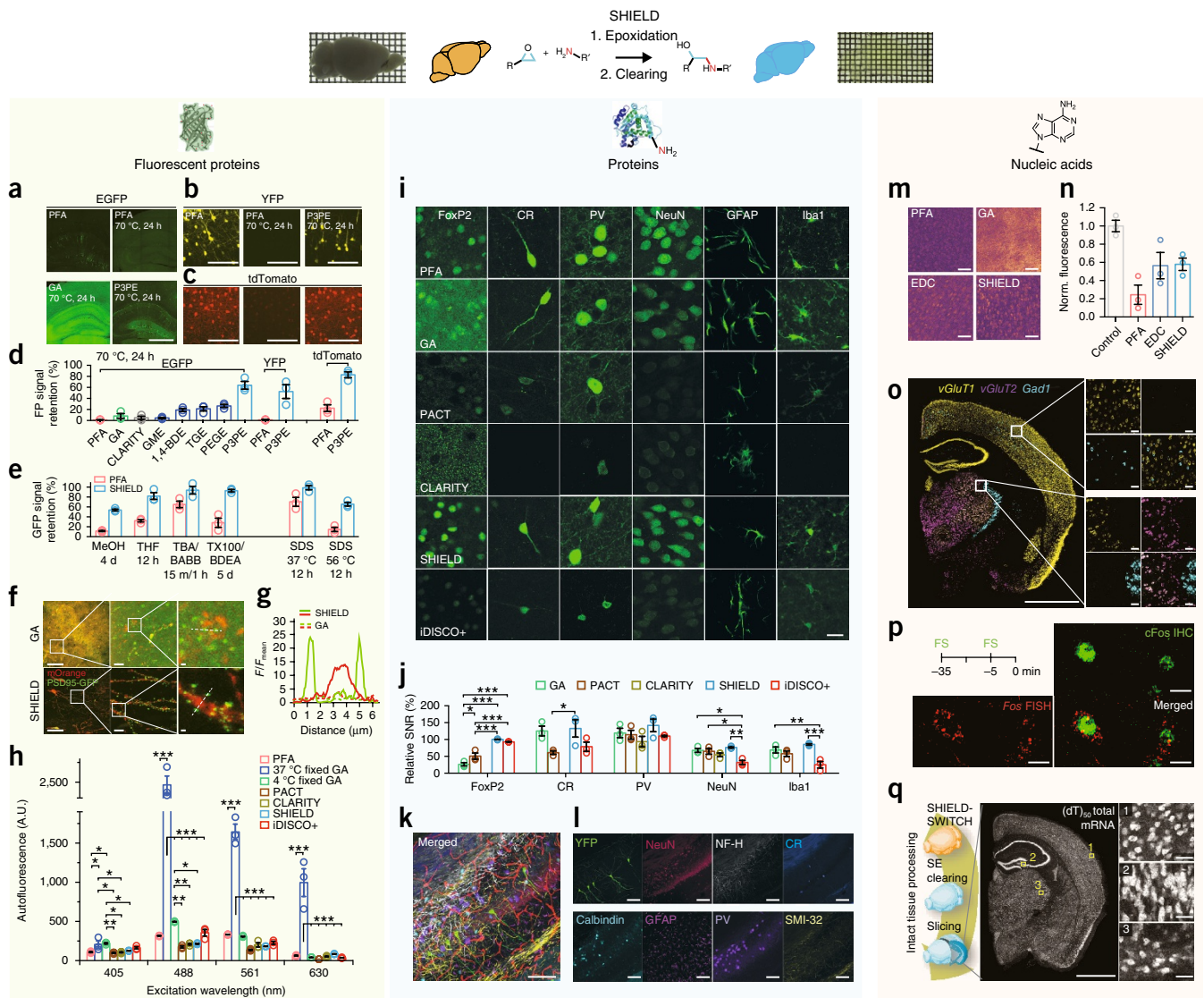

Figure 2 SHIELD preserves fluorescent protein signals, proteins, transcripts and their probe-binding affinities. (**a–c**) Representative fluorescent protein signals of brain slices subjected to thermal treatment after processed with fixatives (PFA, GA or P3PE). Brain slices expressing EGFP (Thy1::EGFP M-line), YFP (Thy1::YFP H-line) or tdTomato (PV-Cre loxP-tdTomato) were used. Scale bars: 1 mm (**a**), 100 μm (**b,c**). (**d**) Fluorescent protein (FP) signal retention after the same heat treatment in brain sections preserved with difference fixatives and CLARITY. $N = 3$ tissue samples. (**e**) GFP signal retention from M-line slices after exposure to organic solvents and detergents. MeOH, methanol; THF, tetrahydrofuran; TBA, *tert*-butyl alcohol; BABB, one part benzyl alcohol and two parts benzyl benzoate; TX100, Triton-X100; BDEA, butyldiethanolamine; SDS, sodium dodecyl sulfate. $N = 3$ tissue samples. (**f**) Fluorescence images of neurons virally labeled with RV-hSyn-mOrange-p2A-PSD95-GFP in GA and SHIELD tissue. Scale bars: 100, 10 and 1 μm (left to right). (**g**) Fluorescence intensity profiles of PSD95-GFP (green) and mOrange (red) signals along the dotted lines in **f**. (**h**) Tissue autofluorescence from various excitation wavelengths; A.U., arbitrary units. $N = 3$ tissue samples. (**i**) Representative images comparing the immunofluorescence of key cell-type antibodies in tissues prepared by various tissue processing methods. Scale bar, 20 μm. FoxP2, forkhead box protein P2; CR, calretinin; PV, parvalbumin; NeuN, neuronal nuclei; GFAP, glial fibrillary acidic protein; Iba1, ionized calcium-binding adaptor molecule 1. The same imaging and display settings were used for each antibody. (**j**) SNRs of immunofluorescence in **i** normalized to the SNR of PFA control. $N = 3$ tissue samples. (**k,l**) SHIELD preserves endogenous YFP fluorescence during multiple rounds of immunostaining and destaining. (**k**) Overlay of multi-round immunostained images. Scale bar, 100 μm. (**l**) Images from individual rounds. Scale bars, 100 μm. (**m**) Representative heat maps of FISH of total mRNAs by (dT)$_{50}$-Cy3 in cleared PFA, EDC-CLARITY, GA and SHIELD tissues. Scale bars, 100 μm. (**n**) Fluorescence intensities of (dT)$_{50}$-Cy3 FISH normalized to the signal of uncleared PFA tissues (control), $N = 3$ tissue samples. (**o**) FISH hybridization chain reaction against three mRNAs in SHIELD tissue: *VGluT1* (*Slc17a7*), *vGluT2* (*Slc17a6*) and *GAD1* (*Gad1*). Scale bars, 2 mm (left) or 100 μm (right). (**p**) Dual labeling of c-Fos protein by immunohistochemistry (IHC) and the corresponding *Fos* mRNA in SHIELD tissue from a mouse foot-shocked (FS) twice at 35 and 5 min before death. Scale bars, 10 μm. (**q**) Uniform preservation of transcripts in a SHIELD-processed brain hemisphere cleared with stochastic electrotransport (SE). See **Supplementary Video 1**. Scale bars, 2 mm (left) or 100 μm (right). Mean ± s.e.m. in all bar graphs. One-way ANOVA, Tukey's multiple comparison test, *$P < 0.05$, **$P < 0.01$, ***$P < 0.001$.
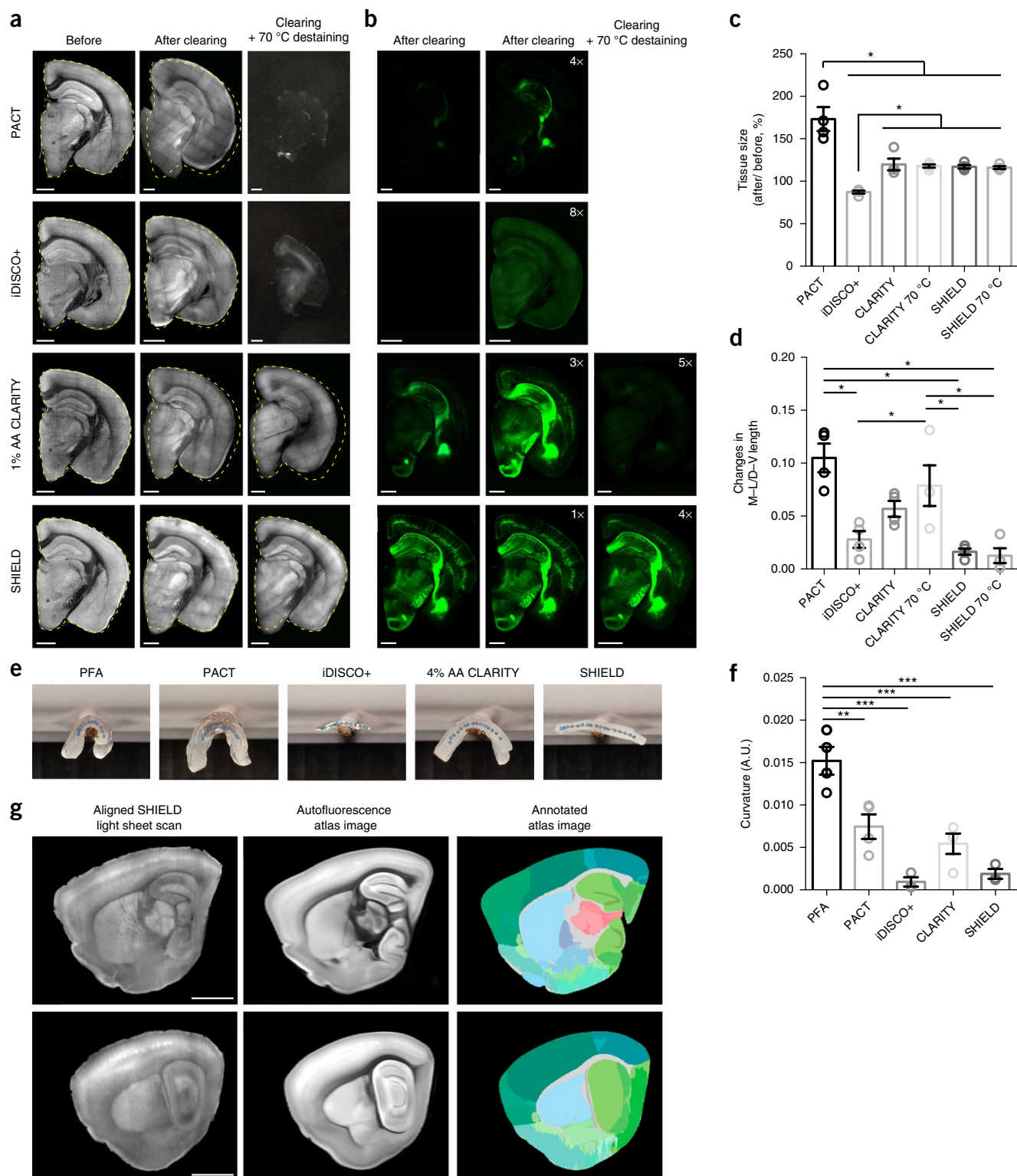
Figure 3 SHIELD protects tissue architecture against physical and chemical stressors. (**a,b**) Autofluorescence (**a**) and YFP (**b**) images of 1-mm-thick brain blocks before and after clearing, and after additional 70 °C destaining step (2 h in 300 mM SDS). The yellow dotted lines mark the original contour of the blocks before clearing. Numbers in YFP images indicate intensity gain by adjusting the display range of the images. Scale bars, 1 mm. (**c**) Tissue size change after delipidation and optical clearing. CLARITY 70 °C indicates 1% acrylamide (AA) CLARITY tissue destained at 70 °C for 2 h after 37 °C delipidation. $N = 4$ tissues. (**d**) Tissue deformation quantified by changes in the ratio of medio-lateral (M–L) and dorso-ventral (D–V) length of individual tissue blocks. $N = 4$ tissue blocks. (**e**) Photos of cleared 1-mm-thick mouse brain sagittal blocks on a rod. Interpolated centerlines of the tissues were marked with dots. (**f**) Quantification of tissue curvature; A.U., arbitrary units. $N = 3$ tissue samples. (**g**) Fully automated registration of autofluorescence images from a SHIELD mouse brain sample to autofluorescence images of the Allen Brain Atlas (© 2015 Allen Institute for Brain Science. Allen Brain Atlas API. Available from: http://brain-map.org/api/index.html). Scale bars, 2 mm. Mean ± s.e.m. for all bar graphs. One-way ANOVA, Tukey's multiple comparison test, $*P < 0.05$, $**P < 0.01$, $***P < 0.001$.

SHIELD enables integrated 3D mapping of the human brain

The controllable reaction kinetics of SHIELD can be further applied to banked clinical samples to obtain a durable tissue gel capable of withstanding multiple rounds of staining and elution. To demonstrate the potential for generating integrated human brain maps using SHIELD, we processed a formalin-fixed 2-mm-thick coronal block of human brain taken at the posterior boundary of the occipital horn of the lateral ventricle (9 cm × 5.5 cm × 0.2 cm, aspect ratio 45:1) and passively cleared it at 80 °C for 10 d (**Fig. 4a,b**). Although gray matters became fully transparent after a few days, we extended the incubation time to completely clear dense white matter. PFA-only and CLARITY tissues became severely damaged and mechanically unstable after full clearing. The high aspect ratio of such disintegrated tissue made it susceptible to additional physical damage during tissue handling. The tissue processed with SHIELD, however, was both transparent and structurally stable. Nuclear and vasculature labeling of the hybrid revealed macroscopic tissue architecture as well as individual cells (**Fig. 4c** and **Supplementary Video 3**).

SHIELD-processed human tissue was compatible with various cell-type and structural markers, and cyto-, chemo- and myeloarchitectural details could be visualized. In cortical tissue, we confirmed the presence of various interneurons, as well as glial cells (**Fig. 4d–i** and **Supplementary Video 4**). In the cerebellum, calbindin staining provided rich morphological details, enabling cell-type classification based on both morphology and protein expression (for example, Purkinje cells) (**Fig. 4f**). We were also able to stain for neurofilament proteins and extracellular matrix protein (**Fig. 4d**). Myelin basic protein staining showed the myeloarchitecture of different brain regions (**Fig. 4f**). In the midbrain, neurofilament-L staining enabled delineation of individual nuclei and brain regions (**Fig. 4e**). Within these parcellated regions, we could probe for cell-type and morphological information by staining for tyrosine hydroxylase (**Fig. 4e**). Taken together, these results show that SHIELD processing facilitates the simultaneous visualization of both structural and cellular features in human brain tissue, enabling integrated 3D human brain mapping at cellular resolution.

SHIELD allows new approaches in tissue phenotyping

We next tested whether SHIELD allows rapid phenotyping of freshly excised biopsies. Microscopic examination of a biopsy has been the gold standard for diagnosis of many diseases[39]. Conventional histology, however, requires laborious and slow processes to formalin-fix, dehydrate, paraffin-embed, section and stain tissue samples. Relatively few of the slices produced by sectioning are imaged. The resulting sparse sampling and loss of volumetric information can limit diagnostic accuracy. Recent advances in tissue clearing techniques have enabled more holistic, volumetric imaging of intact biopsies[40–42]. These methods, however, rely on slow diffusion of chemicals and therefore become increasingly inefficient as the size of the biopsy increases.

SHIELD combined with stochastic electrotransport can preserve, clear and immunolabel intact needle biopsies within 4 h (**Fig. 5a–e**). The controllable SHIELD reaction kinetics enabled rapid conversion of a fresh biopsy sample into a clearable tissue-gel (**Fig. 5a,b**). We then used stochastic electrotransport to rapidly clear and uniformly label the intact sample with a vasculature marker and an antibody within 2 h (**Fig. 5c,d** and **Supplementary Video 5**). This pipeline is also applicable to PFA-fixed tissues. For example, we were able to visualize proliferating Ki-67–positive cells and vasculature in a PFA-fixed mouse kidney harboring breast cancer metastasis (**Fig. 5e** and **Supplementary Video 6**). Taken together, these results demonstrate

that a SHIELD-based pipeline may enable rapid 3D phenotyping of intact biopsy samples.

Combining SHIELD with MAP (magnified analysis of the proteome) allows interrogation of fine structural and molecular features across large tissue volumes (**Fig. 5f–o**). Although MAP enables super-resolution imaging of millimeter-thick samples with diffraction-limited microscopes[13], the harsh treatment required for isotropic expansion causes loss of fluorescent protein signal. Therefore, additional immunolabeling is necessary to image features tagged with fluorescent proteins. We discovered that an interpenetrating dense hydrogel can mechanically expand SHIELD-processed tissue isotropically by threefold without the need for harsh treatment (**Fig. 5f–l**) while effectively preserving signal from fluorescent proteins (**Figs. 5g** and **6**). Distortion analysis of GFP-positive neurons before and after expansion showed less than 4% error across multiple length scales (**Fig. 5h,i**), which is comparable to results from previous expansion protocols[13,19,43]. Morphological details of dendritic spines were also well preserved after expansion (**Fig. 5j–l**).

SHIELD-MAP enabled super-resolution imaging of fine subcellular architecture labeled with fluorescent proteins in millimeter-thick samples. Traditionally, imaging and volumetric reconstruction of synaptic input fields or dendritic arborization has been limited to specific classes of neurons confined to a small volume because it requires imaging with high numerical aperture (NA) objectives (NA 1.4) with a short working distance (200–300 μm)[44,45]. SHIELD-MAP extends such studies to a wider range of neuronal types by enabling super-resolution imaging of signal from fluorescent proteins in tissue that is an order of magnitude thicker using medium-NA (1.0) objectives with a long working distance (8 mm). We demonstrated imaging of dendritic spines expressing fluorescent protein in 5-mm-thick mouse brain tissue after expansion (**Fig. 5m,n** and **Supplementary Video 7**). Negligible loss of resolution and high fluorescent protein signal enabled the extraction of fine morphological features throughout the entire depth of the sample (**Fig. 5n**) and the reconstruction of the dendritic arborization of a single neuron spanning a large tissue volume (**Fig. 5o** and **Supplementary Video 8**).

Integrated cellular-resolution circuit mapping

We next applied SHIELD to comprehensively characterize a genetically defined neural circuit. The GPe is a major relay in the indirect pathway in the basal ganglia[46] and is thought to play a role in voluntary movements and movement disorders such as dystonia and Parkinson's disease[47]. About 40% of neurons in the GPe are PV+ (ref. 48), and their projections to several basal ganglia nuclei have been identified. However, it remains unclear how individual PV+ neurons in the GPe (GPe-PV+ neurons) project to multiple target areas at the single-cell level. SHIELD combined with viral labeling tools might enable integrated mapping of GPe-PV+ long-range output, downstream target cells, and those cells' molecular properties at single-cell resolution.

To test this possibility, we targeted GPe-PV+ neurons by injecting AAV-flex-mRuby2-Synaptophysin-EGFP virus into a PV-Cre transgenic mouse brain (**Fig. 6a**), which labeled neurites with mRuby2 and presynaptic boutons with EGFP[49]. We SHIELD-processed and stochastic electrotransport–cleared an intact mouse brain hemisphere, and imaged it using a light-sheet microscope (**Supplementary Table 3**) to map the global projection pattern of GPe-PV+ neurons (**Fig. 6a–d** and **Supplementary Video 9**). Negligible tissue distortion and fluorescent protein signal loss enabled automated atlas alignment, region segmentation and fluorescent protein signal detection (**Fig. 6c,d**). We found GFP-labeled synaptic terminals in the GPe, subthalamic
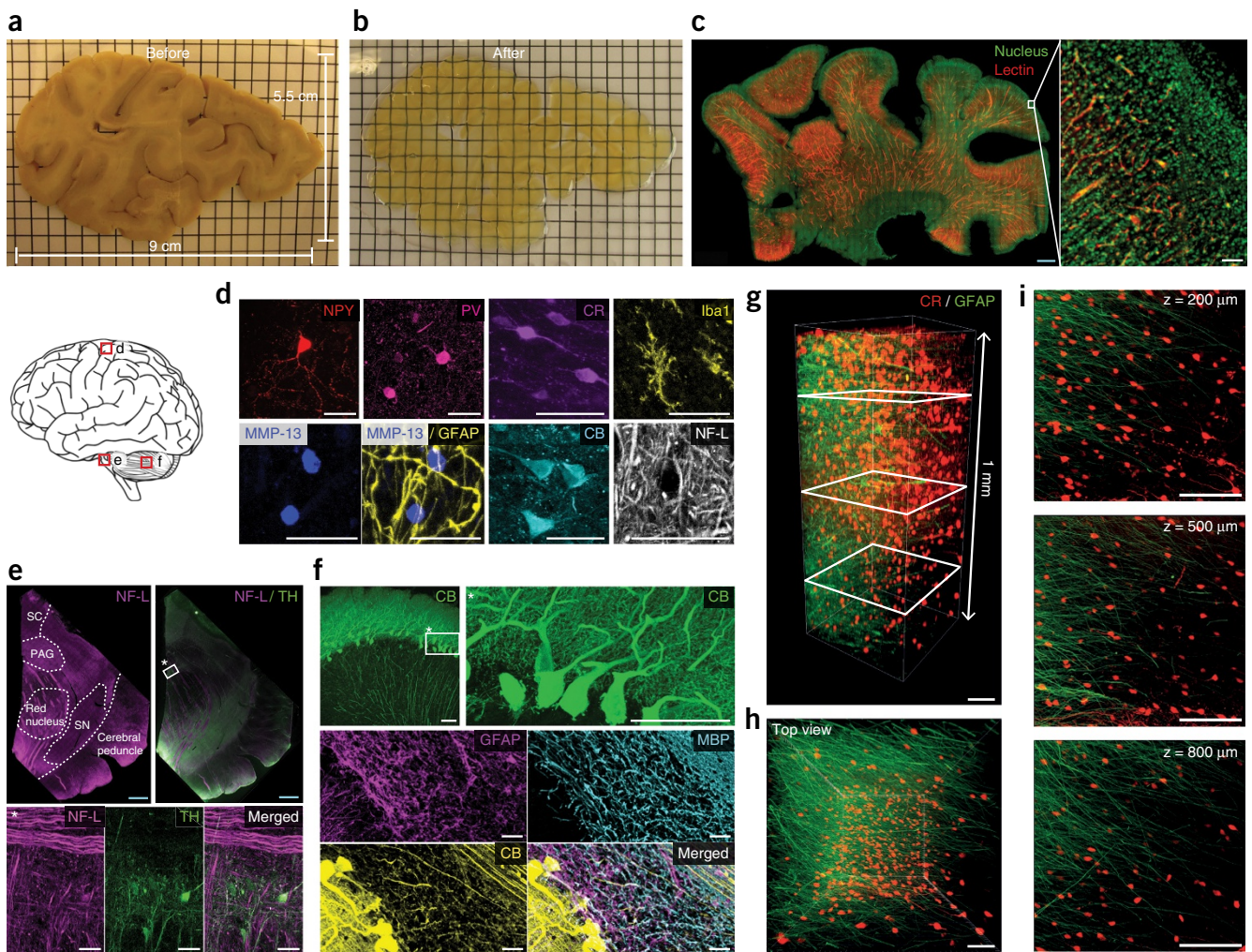
Figure 4 SHIELD enables 3D imaging of various structures and cell types and their morphological details in human brain tissue. (**a**,**b**) A 2-mm-thick slab of human brain coronal hemisphere (9 cm × 5.5 cm × 2 mm) before (**a**) and after (**b**) SHIELD processing. Grid, 5 mm. (**c**) A SHIELD-processed slab (22 mm × 38 mm × 1.3 mm) was stained with lectin and nuclear dye, and the 800-μm-thick volume from the top surface was imaged with a custom-built, temporally focused line-scanning two-photon microscope. Scale bars: 2 mm (blue, left) or 100 μm (white). See **Supplementary Video 3**. (**d**–**f**) Immunostained cortex (**d**), midbrain (**e**) and cerebellum (**f**) from 100-μm-thick SHIELD-processed human brain tissues, showing various cell types and structures. In **e**, neurofilament-L (NF-L) staining assists delineation of midbrain areas. NPY, neuropeptide Y; CR, calretinin; Iba1, ionized calcium-binding adaptor molecule 1; MMP-13, matrix metallopeptidase 13; GFAP, glial fibrillary acidic protein; CB, calbindin; MBP, myelin basic protein; TH, tyrosine hydroxylase; SC, superior colliculus; PAG, periaqueductal gray; SN, substantia nigra. Scale bars: 2 mm (blue, top row in **e**) or 50 μm (white). (**g**–**i**) GFAP (green) and CR (red) immunolabeling of a SHIELD-processed 1-mm-thick human cortex coronal block. See **Supplementary Video 4**. (**g**) 3D reconstruction. Scale bar, 100 μm. (**h**) Top view of the 3D reconstruction. Scale bar, 100 μm. (**i**) Maximum-intensity projection images at various z positions (200, 500 and 800 μm) marked by white rectangles in **g**. For maximum-intensity projection, 100-μm-thick z stacks were used at each z position. Scale bars, 100 μm.

nucleus (STN), substantia nigra reticulata (SNr), globus pallidus interna (GPi), nucleus reticularis thalami (nRT), caudate putamen (CPu) and parafascicular nucleus (PF) (**Fig. 6b**–**d**).

To further investigate the PV-GPe circuit, we dissected a 1-mm-thick tissue block that included the GPe, STN, nRT, GPi and SNr. We then performed FISH followed by delabeling and immunostaining to map *Gad1* mRNA and calretinin protein (**Fig. 6a**,**e** and **Supplementary Video 10**). Finally, the tissue was expanded using SHIELD-MAP for super-resolution imaging (**Fig. 6a**,**e**).

All GPe-mRuby2^{+} neurons were *Gad1*^{+} and had synaptophysin-EGFP (Syp-EGFP[+]) puncta on their somata, suggesting putative axosomatic connectivity among GPe-PV^{+} neurons. To characterize

the long-range output of a GPe-PV[+] neuron at single-cell resolution, we reconstructed the axonal arborization of an mRuby2[+] neuron (**Fig. 6e**,**f**). The preservation of fluorescent protein signal and enhanced resolution obtained with SHIELD-MAP allowed reliable reconstruction of individual axons and their presynaptic boutons (**Fig. 6e**–**i** and **Supplementary Video 11**). Negligible tissue damage and the isotropic expansion enabled integration of the molecular features acquired from the FISH and immunostaining rounds into the axogram (**Fig. 6f**,**g**), which allowed molecular characterization of the traced neuron and its downstream targets (**Fig. 6f**–**m**).

The resulting multidimensional axogram suggested that the reconstructed neuron might be connected to 4 neurons in the GPe,
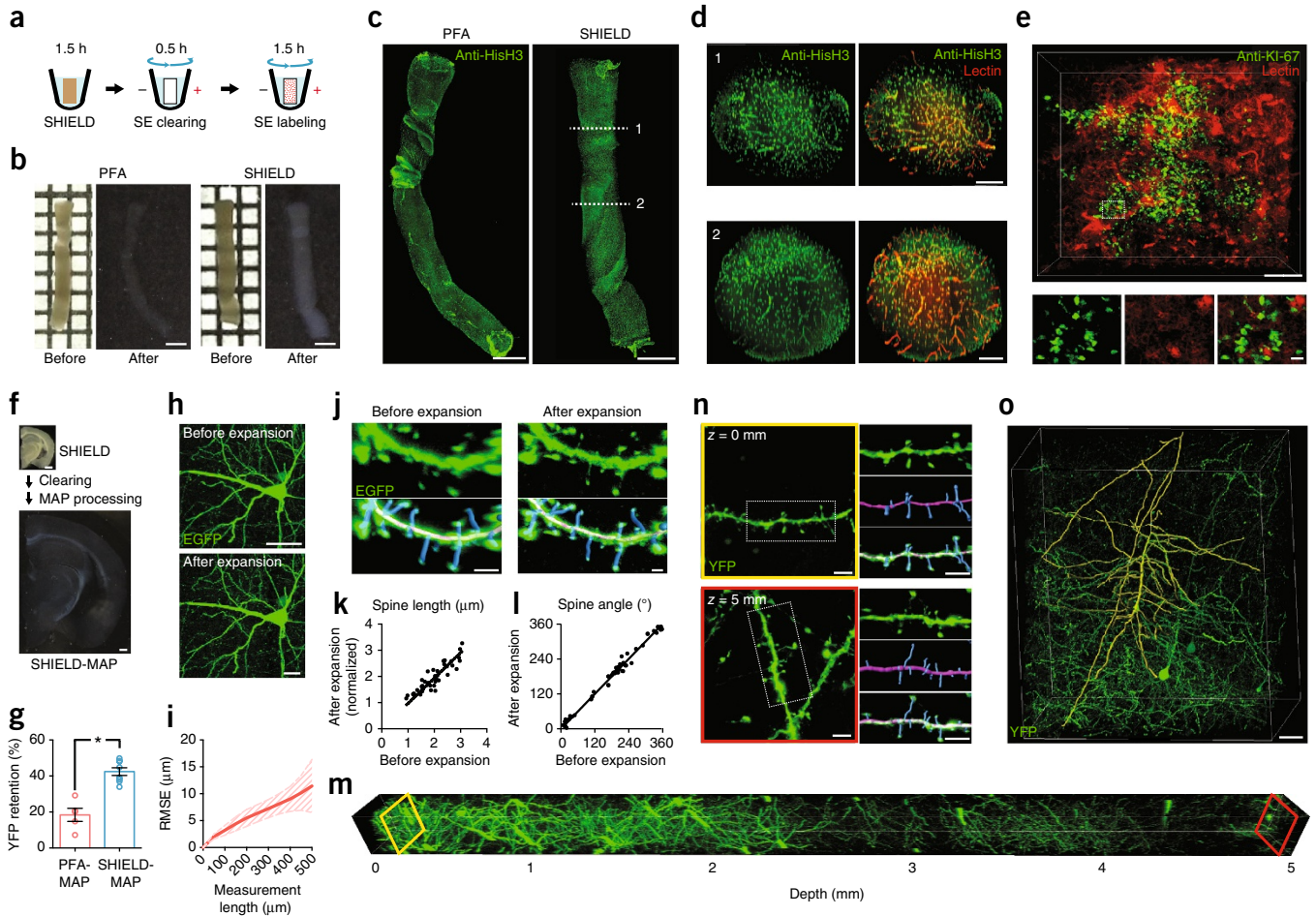
Figure 5 SHIELD enables new tissue phenotyping approaches. (**a–e**) Ultrafast 3D molecular phenotyping of an intact needle biopsy. (**a**) Pipeline. SE, stochastic electrotransport. (**b**) Morphological preservation of a fresh brain biopsy by SHIELD after clearing. Grid, 1 mm; scale bars, 1 mm. (**c**) Complete immunolabeling and visualization of intact biopsy samples with histone H3 antibody (anti-HisH3). Scale bars, 1 mm. See **Supplementary Video 5**. (**d**) Cross-sectional images of sample in **c**. Note that antibody and lectin signal is uniform throughout the entire volume. Scale bars, 200 μm. (**e**) A mouse kidney biopsy harboring breast cancer metastasis was rapidly processed and stained for a cancer cell marker (anti-Ki-67). Scale bars: 200 μm (top), 20 μm (bottom, enlarged images). See **Supplementary Video 6**. (**f–o**) Super-resolution imaging of endogenous fluorescent protein signal in large tissue volumes by SHIELD-MAP. (**f**) SHIELD-MAP pipeline and processed tissue images. Scale bars, 1 mm. (**g**) Fluorescence retention after PFA-MAP without denaturation and SHIELD-MAP. $N = 4$ tissue samples. Mean ± s.e.m. (**h**) Images showing a GFP-expressing neuron before (top) and after (bottom) SHIELD-MAP processing and expansion. Scale bars, 50 μm. (**i**) Root-mean-squared measurement error (RMSE) of the images before and after SHIELD-MAP processing and expansion (red line, mean; filled area, s.d.; $N = 4$ tissue samples). (**j**) Images showing segmented EGFP-expressing dendritic spines (blue) before and after SHIELD-MAP expansion. Scale bars, 2 μm. (**k,l**) SHIELD-MAP preserves morphological features of the spine, such as length (**k**) and angle (**l**). Spine length after expansion is normalized by the tissue expansion ratio. Linear regression, $R^2 = 0.7764$ (**k**) and $R^2 = 0.9879$ (**l**). $N = 49$ and 62 spines for **k** and **l**, respectively. (**m,n**) Volumetric imaging of 5-mm-thick expanded SHIELD-MAP tissue. See **Supplementary Video 7**. (**n**) Images showing segmented dendrites (magenta) and spines (blue) from the tissue surface (top) and at a depth of 5 mm (bottom; 1.67 mm before expansion). Scale bars, 10 μm. (**o**) Reconstructed dendrites (yellow) of a cortical Thy1-YFP+ neuron. Scale bar, 200 μm. See **Supplementary Video 8**. Unpaired *t*-test, *$P < 0.05$.

2 neurons in the nRT and 13 neurons in the SNr through putative axosomatic synapses (**Fig. 6f**). Most of the downstream targets were *Gad1*+. In the SNr, all downstream targets of this neuron were CR− despite the finding that 22% of SNr neurons with EGFP+ axosomatic boutons were CR+ (**Fig. 6k**). Eighty-five percent of Syp-EGFP+ SNr neurons were *Gad1*+ (**Fig. 6j**).

We found that the reconstructed neuron innervated the STN through three different axon collaterals originating from two axon hillocks (**Fig. 6e,f**). Collaterals to the nRT or SNr were from a single axon hillock (**Fig. 6e,f**). Statistical analysis of presynaptic ultrastructure revealed the number of bifurcations near the target neuronal soma to be positively correlated with the total number of axosomatic

boutons (**Fig. 6l**). A subset of *Gad1*+ SNr neurons received putative axosomatic inputs from multiple collaterals bifurcating far from their target soma (92.2 ± 16.1 μm linear distance before expansion, $N = 3$ cases) (**Fig. 6f–i**). These data show that SHIELD together with MAP enables integrated multiscale circuit mapping with unprecedented resolution and accuracy. This approach may provide an anatomical framework for understanding neural circuit mechanisms.

DISCUSSION

In this study, we identified a polyepoxide for advanced tissue processing that possesses several key properties, including polyfunctional reactive groups with a flexible backbone for the formation of intra- and

Figure 6 SHIELD enables integrated circuit reconstruction at single cell resolution. (**a**) Pipeline. (**b**) 3D rendering of the intact mouse hemisphere showing brain-wide projection patterns of labeled GPe-PV+ neurons. See **Supplementary Video 9**. Scale bar, 1 mm. (**c**) Representative images of labeled neurons and their presynaptic terminals in GPe, STN, SNr and GPi. Scale bars, 100 µm. (**d**) Total pixel intensity of mRuby2 and EGFP in seven brain regions to which the labeled GPe-PV+ neurons project. CPu, caudate putamen; PF, parafascicular nucleus; A.U., arbitrary units. (**e**) 3D rendering of labeled GPe-PV+ neuronal circuitry with the overlaid axon trace of a single labeled neuron. The inset shows example images from multiround staining and multiscale imaging. Main scale bar, 1 mm; insets, 50 µm. IHC, immunohistochemistry. (**f**) Reconstructed axon arborization of the neuron and its downstream targets. Each circle represents a neuron. The number of putative axosomatic boutons is marked inside each circle. (**g**) Images of the circuit components from multiround imaging. Arrows indicate the target cell body. Scale bars, 20 µm. (**h**) Reconstructed putative axosomatic connectivity. Ramified axons (gray) and EGFP+ presynaptic boutons (blue) are segmented. Scale bars, 20 µm. (**i**) Convergence of two axon collaterals branched remote from the target cell body. See **Supplementary Video 11** for a 3D reconstruction of this connectivity. Scale bars, 20 µm. (**j**,**k**) Venn diagram showing three different neuronal populations in the SNr. (**j**) $Gad1^+$ Syp-EGFP$^-$, $Gad1^+$ Syp-EGFP$^+$, and $Gad1^-$ Syp-EGFP$^+$. (**k**) CR$^+$ Syp-EGFP$^-$, CR$^+$ Syp-EGFP$^+$, and CR$^-$ Syp-EGFP$^+$. Unbiased sampling was used for this quantification. (**l**) A relationship between the number of axosomatic boutons and the axonal branching events of the reconstructed PV-mRuby2$^+$ neuron near the target neuronal soma. Linear regression, $R^2 = 0.55$, F-test, $F_{1,14} = 17.40$, $P = 0.0009$. $N = 11$ connections. (**m**) The distribution of the number of putative axosomatic boutons.

intermolecular bonds, reactivity to various classes of biomolecules, and tightly controllable reaction kinetics under mild conditions. By promoting multipoint intramolecular fluorescent protein cross-links, SHIELD safeguards fluorescent protein signal against harsh conditions commonly used in many tissue phenotyping methods. Controlled tissue epoxidation effectively cross-links both proteins and nucleic acids while preserving their probe-binding affinities to various commercially available antibodies and FISH reagents. Epoxidation also protects tissue architecture during delipidation and destaining.

SHIELD combined with SWITCH can effectively preserve endogenous molecules, protein fluorescence and tissue architecture uniformly in both intact mouse hemispheres and long-banked clinical samples. SWITCH ensures uniform dispersion of polyepoxide throughout a large-scale sample before the synchronized initiation of the epoxidation reaction, enabling the preservation of tissue-wide physicochemical properties. Key parameters (for example, incubation time) of SWITCH-mediated tissue epoxidation will, however, need to be optimized for different types of samples.

Recently, tissue-clearing techniques have been applied to biopsy samples to demonstrate the potential of 3D pathology approaches to improve the diagnosis and treatment of cancer[40–42]. These benefits, however, were moderated by a lengthy processing time or potential damage to tissue architecture. By contrast, the SHIELD and stochastic electrotransport processing pipeline enabled 3D molecular phenotyping of intact needle biopsies with very high speed (4 h for a 1-mm-diameter biopsy). This pipeline could be used to quickly determine a tumor's subtype and heterogeneity in clinical labs when timely treatment is required.

Recent advances in viral labeling, tissue processing and imaging technologies have enabled mapping of long-range wiring in mouse brains[50–52]. For instance, Ye et al.[50] demonstrated brain-wide mapping of axonal bundle projections using CLARITY. Economo et al.[51] developed a platform for brain-wide imaging and reconstruction
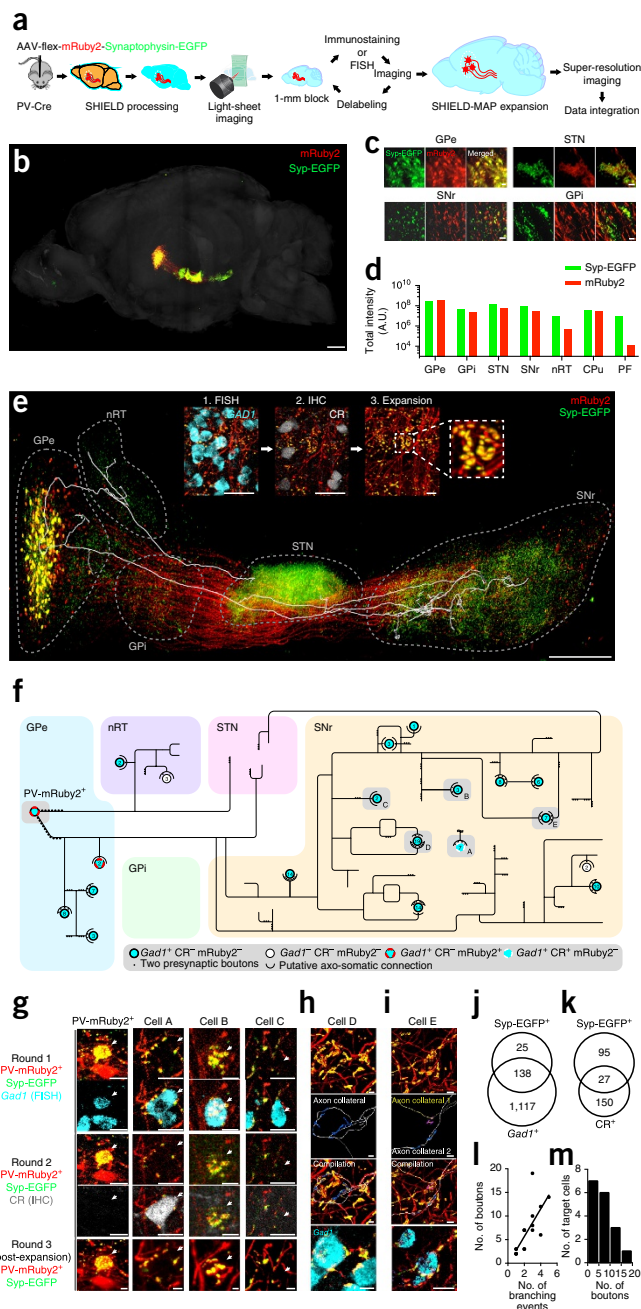
of long-range axonal arbors at single-fiber resolution using partial tissue clearing and a high-speed two-photon microscope integrated with a tissue vibratome. However, molecular phenotyping of the very same cells with known axonal projection pattern and identifying their downstream target cells, which is crucial in understanding cell function, remains challenging.

When combined with genetic and viral tools, SHIELD may serve as a powerful platform for integrated multiscale interrogation of neural circuits. The high level of fluorescent protein preservation in SHIELD and SHIELD-MAP enabled repeated imaging of fluorescent protein–labeled neuronal structures across multiple scales, from whole brain to submicron architectures (for example, synaptic puncta). We demonstrated that global projection patterns can be mapped using SHIELD followed by SHIELD-MAP for

super-resolution imaging of regions of interest in the same brain to reconstruct individual axonal projections and synaptic structures. Thanks to high fluorescent protein signal and low background, we were able to use low laser power to image multiple fluorescent proteins repeatedly with minimal photobleaching. Even though SHIELD-MAP decreases fluorescent protein density by 27-fold owing to threefold linear expansion, we were still able to clearly and rapidly image both fluorescent protein–labeled axonal fibers and presynaptic puncta.

SHIELD and SHIELD-MAP enable extraction and integration of brain-wide wiring, single-cell-resolution axograms, and the molecular features of downstream neurons from the same brain. To demonstrate, we reconstructed the axogram of a GPe-PV$^+$ neuron, including its axon arborization patterns and molecular details of its downstream targets, and their putative axosomatic connectivity with presynaptic bouton numbers. We claim only putative axosomatic connectivity because we used presynaptic boutons adjacent to somata as the sole indicator of neuron-to-neuron connection. Additional multiplexing with postsynaptic proteins (for example, PSD95) and dendritic proteins (for example, MAP2) may allow more precise mapping of synaptic connections using SHIELD.

We anticipate that existing tissue phenotyping methods requiring unphysiological treatment will benefit from SHIELD, as it protects biological tissue against a wide range of stressors. The integration of SHIELD with other protocols may, however, require systematic optimization because tissue epoxidation changes the degree of structural and molecular preservation, which subsequently affects downstream processing. For example, SHIELD treatment increases the amount of biomolecule and structural feature preservation, which can decrease tissue permeability and slow molecular transport. Therefore, subsequent steps that require molecular transport will need to be optimized.

Penetration depth of molecular probes in SHIELD tissue is dependent on tissue type, specimen size, and copy number and distribution patterns of target molecules. SHIELD enables high-SNR imaging of a wide range of biomolecules thanks to a minimal loss of endogenous molecules and their probe binding affinities. To avoid depletion of molecular probes by high-copy-number targets, we recommend using SWITCH to control probe–target binding kinetics. Stochastic electrotransport further enhances speed and uniformity of labeling in various types of tissues and organs[28]. The processing time and the required probe amount would need to be empirically determined for each target and sample type, as in all other tissue phenotyping methods.

SHIELD in combination with DNA and RNA FISH approaches can facilitate spatial genomics[53,54] and the integration of single-cell sequencing analysis into a 3D cell map of model systems and clinical samples[7]. SHIELD can also be used for volumetric mapping of gene expression profiles in whole-mount intact tissues at single-cell resolution using multiplexed FISH techniques[53,54].

Polyepoxide and other multifunctional cross-linkers have been widely used in various industries as coating resins, adhesives and embedding media for electron microscopy[55]. A large library of multifunctional cross-linkers is available, and new chemicals with different functionalities are currently being developed. We envisage rationally guided screening or design of new multifunctional cross-linkers further enhancing the utility of the SHIELD approach.

The versatility of SHIELD combines many advantages of existing methods into a simple, scalable and broadly applicable protocol. SHIELD synergizes with a wide range of technologies and will enable new integrated approaches for studying complex biological systems.

Editor's note: Before publication, the editors were made aware of a dispute concerning the order of authorship. Specifically, Margaret McCue claimed that her contributions to the paper warranted joint first authorship alongside Young-Gyun Park, Chang Ho Sohn and Ritchie Chen. At the request of the Office of the MIT Dean of Engineering, two MIT faculty members, from the Department of Chemical Engineering and the Institute for Medical Engineering & Science, conducted a review of the contributions of the authors to the work presented in the paper. They concluded that the position of Ms. McCue as a second author was an appropriate reflection of her contributions. Ms. McCue maintains that her contributions warrant inclusion as a first author.

METHODS
Methods, including statements of data availability and any associated accession codes and references, are available in the online version of the paper.

Note: Any Supplementary Information and Source Data files are available in the online version of the paper.

AUTHOR CONTRIBUTIONS
K.C. conceived the idea. Y.-G.P., C.H.S., R.C., D.H.Y., and K.C. designed the experiments and wrote the paper with input from other authors. Y.-G.P. led development of SHIELD-SWITCH and SHIELD-MAP methods. H.J.K and H.W.Q. performed the molecular simulation in Figure 1. R.C. performed the physicochemical analysis in Figure 1 and quantified the fluorescence preservation in Figure 2. R.C. and M.M. performed fluorescent protein experiments in Figure 2. M.M. and R.C. acquired and analyzed the virus-labeled neuronal images in Figure 2. C.H.S. and Y.-G.P. performed the immunoreactivity experiments and autofluorescence quantification in Figure 2. R.C. performed the multi-round immunostaining in Figure 2. C.H.S. and R.C. designed and performed the FISH experiments and protein analyses. Y.-G.P. and C.H.S. characterized physical properties of SHIELD tissue in Figure 3. C.H.S. and G.D. designed SHIELD processing for postmortem human brain tissues and performed immunostaining in Figure 4. H.C. built temporally focused line-scanning microscope and acquired the large human brain slab image in Figure 4. D.H.Y. and Y.-G.P. established the pipeline for 3D phenotyping of the biopsy samples in Figure 5. T.K. performed the isotropic expansion analysis in Figure 5 and contributed to the development of SHIELD-MAP method. N.B.E. conducted light-sheet microscope imaging in Figure 6. Y.-G.P. and C.H.S. performed neuronal fiber tracing, and Y.-G.P performed imaging and analysis in Figure 6. H.C.O. and W.T. helped sample preparation. M.C.T. and H.L.P. provided purified GFP. X.J. and T.R.G. provided tumor tissues. S.C. and J.W. developed the oscillating blade microtome. M.P.F provided human brain tissues and validated the human brain data. V.L. and B.K.L. provided the virus, the virus labeled tissues, and helpful discussion. K.C. supervised all aspects of the work.

COMPETING INTERESTS

K.C. is a co-inventor on patent application owned by MIT covering the SHIELD and SWITCH technology (PCT/US2016/064538).

Reprints and permissions information is available online at http://www.nature.com/reprints/index.html. Publisher's note: Springer Nature remains neutral with regard to jurisdictional claims in published maps and institutional affiliations.

1. Masland, R.H. Neuronal cell types. *Curr. Biol.* **14**, R497–R500 (2004).
2. Kepecs, A. & Fishell, G. Interneuron cell types are fit to function. *Nature* **505**, 318–326 (2014).
3. Alivisatos, A.P. *et al.* The brain activity map. *Science* **339**, 1284–1285 (2013).
4. DeFelipe, J. From the connectome to the synaptome: an epic love story. *Science* **330**, 1198–1201 (2010).
5. Zingg, B. *et al.* Neural networks of the mouse neocortex. *Cell* **156**, 1096–1111 (2014).
6. Kasthuri, N. *et al.* Saturated reconstruction of a volume of neocortex. *Cell* **162**, 648–661 (2015).
7. Crosetto, N., Bienko, M. & van Oudenaarden, A. Spatially resolved transcriptomics and beyond. *Nat. Rev. Genet.* **16**, 57–66 (2015).
8. Shah, S., Lubeck, E., Zhou, W. & Cai, L. In situ transcription profiling of single cells reveals spatial organization of cells in the mouse hippocampus. *Neuron* **92**, 342–357 (2016).
9. Giesen, C. *et al.* Highly multiplexed imaging of tumor tissues with subcellular resolution by mass cytometry. *Nat. Methods* **11**, 417–422 (2014).
10. Chung, K. *et al.* Structural and molecular interrogation of intact biological systems. *Nature* **497**, 332–337 (2013).
11. Susaki, E.A. & Ueda, H.R. Whole-body and whole-organ clearing and imaging techniques with single-cell resolution: toward organism-level systems biology in mammals. *Cell Chem. Biol.* **23**, 137–157 (2016).
12. Sylwestrak, E.L., Rajasethupathy, P., Wright, M.A., Jaffe, A. & Deisseroth, K. Multiplexed intact-tissue transcriptional analysis at cellular resolution. *Cell* **164**, 792–804 (2016).
13. Ku, T. *et al.* Multiplexed and scalable super-resolution imaging of three-dimensional protein localization in size-adjustable tissues. *Nat. Biotechnol.* **34**, 973–981 (2016).
14. Murray, E. *et al.* Simple, scalable proteomic imaging for high-dimensional profiling of intact systems. *Cell* **163**, 1500–1514 (2015).
15. Renier, N. *et al.* iDISCO: a simple, rapid method to immunolabel large tissue samples for volume imaging. *Cell* **159**, 896–910 (2014).
16. Pan, C. *et al.* Shrinkage-mediated imaging of entire organs and organisms using uDISCO. *Nat. Methods* **13**, 859–867 (2016).
17. Tainaka, K., Kuno, A., Kubota, S.I., Murakami, T. & Ueda, H.R. Chemical principles in tissue clearing and staining protocols for whole-body cell profiling. *Annu. Rev. Cell Dev. Biol.* **32**, 713–741 (2016).
18. Ertürk, A. *et al.* Three-dimensional imaging of solvent-cleared organs using 3DISCO. *Nat. Protoc.* **7**, 1983–1995 (2012).
19. Chen, F., Tillberg, P.W. & Boyden, E.S. Expansion microscopy. *Science* **347**, 543–548 (2015).
20. Vincek, V., Nassiri, M., Nadji, M. & Morales, A.R. A tissue fixative that protects macromolecules (DNA, RNA, and protein) and histomorphology in clinical samples. *Lab. Invest.* **83**, 1427–1435 (2003).
21. Pelegri-O'Day, E.M., Lin, E.W. & Maynard, H.D. Therapeutic protein-polymer conjugates: advancing beyond PEGylation. *J. Am. Chem. Soc.* **136**, 14323–14332 (2014).
22. Kabanov, A.V. & Vinogradov, S.V. Nanogels as pharmaceutical carriers: finite networks of infinite capabilities. *Angew. Chem. Int. Ed. Engl.* **48**, 5418–5429 (2009).
23. Sheldon, R.A. & van Pelt, S. Enzyme immobilisation in biocatalysis: why, what and how. *Chem. Soc. Rev.* **42**, 6223–6235 (2013).
24. Hartmann, M. Ordered mesoporous materials for bioadsorption and biocatalysis. *Chem. Mater.* **17**, 4577–4593 (2005).
25. Mateo, C. *et al.* Some special features of glyoxyl supports to immobilize proteins. *Enzyme Microb. Technol.* **37**, 456–462 (2005).
26. Migneault, I., Dartiguenave, C., Bertrand, M.J. & Waldron, K.C. Glutaraldehyde: behavior in aqueous solution, reaction with proteins, and application to enzyme crosslinking. *Biotechniques* **37**, 790–796, 798–802 (2004).
27. Tsien, R.Y. The green fluorescent protein. *Annu. Rev. Biochem.* **67**, 509–544 (1998).
28. Kim, S.-Y. *et al.* Stochastic electrotransport selectively enhances the transport of highly electromobile molecules. *Proc. Natl. Acad. Sci. USA* **112**, E6274–E6283 (2015).
29. Tsien, R.Y. Fluorescent probes of cell signaling. *Annu. Rev. Neurosci.* **12**, 227–253 (1989).
30. Back, J.F., Oakenfull, D. & Smith, M.B. Increased thermal stability of proteins in the presence of sugars and polyols. *Biochemistry* **18**, 5191–5196 (1979).
31. Mason, J.T. & O'Leary, T.J. Effects of formaldehyde fixation on protein secondary structure: a calorimetric and infrared spectroscopic investigation. *J. Histochem. Cytochem.* **39**, 225–229 (1991).
32. Enoki, S., Saeki, K., Maki, K. & Kuwajima, K. Acid denaturation and refolding of green fluorescent protein. *Biochemistry* **43**, 14238–14248 (2004).
33. Fowler, C.B., Evers, D.L., O'Leary, T.J. & Mason, J.T. Antigen retrieval causes protein unfolding: evidence for a linear epitope model of recovered immunoreactivity. *J. Histochem. Cytochem.* **59**, 366–381 (2011).
34. Hama, H. *et al.* Scale: a chemical approach for fluorescence imaging and reconstruction of transparent mouse brain. *Nat. Neurosci.* **14**, 1481–1488 (2011).
35. Hopwood, D. Theoretical and practical aspects of glutaraldehyde fixation. *Histochem. J.* **4**, 267–303 (1972).
36. Lee, K., Choi, S., Yang, C., Wu, H.-C. & Yu, J. Autofluorescence generation and elimination: a lesson from glutaraldehyde. *Chem. Commun. (Camb.)* **49**, 3028–3030 (2013).
37. Deforce, D.L.D., Ryniers, F.P.K., van den Eeckhout, E.G., Lemière, F. & Esmans, E.L. Analysis of DNA adducts in DNA hydrolysates by capillary zone electrophoresis and capillary zone electrophoresis-electrospray mass spectrometry. *Anal. Chem.* **68**, 3575–3584 (1996).
38. Pena, J.T.G. *et al.* miRNA in situ hybridization in formaldehyde and EDC-fixed tissues. *Nat. Methods* **6**, 139–141 (2009).
39. Pappa, V.I. *et al.* Role of image-guided core-needle biopsy in the management of patients with lymphoma. *J. Clin. Oncol.* **14**, 2427–2430 (1996).
40. Nojima, S. *et al.* CUBIC pathology: three-dimensional imaging for pathological diagnosis. *Sci. Rep.* **7**, 9269 (2017).
41. Tanaka, N. *et al.* Whole-tissue biopsy phenotyping of three-dimensional tumours reveals patterns of cancer heterogeneity. *Nat. Biomed. Eng.* **1**, 796–806 (2017).
42. Glaser, A.K. *et al.* Light-sheet microscopy for slide-free non-destructive pathology of large clinical specimens. *Nat. Biomed. Eng.* **1**, 1–10 (2017).
43. Tillberg, P.W. *et al.* Protein-retention expansion microscopy of cells and tissues labeled using standard fluorescent proteins and antibodies. *Nat. Biotechnol.* **34**, 987–992 (2016).
44. Dumitriu, D., Rodriguez, A. & Morrison, J.H. High-throughput, detailed, cell-specific neuroanatomy of dendritic spines using microinjection and confocal microscopy. *Nat. Protoc.* **6**, 1391–1411 (2011).
45. Ke, M.-T. Super-resolution mapping of neuronal circuitry with an index-optimized clearing agent. *Cell Rep.* **14**, 2718–2732 (2016).
46. Gerfen, C.R. & Wilson, C.J. in *Handbook of Chemical Neuroanatomy* **12**, 371–468 (Elsevier, 1996).
47. Obeso, J.A., Rodriguez-Oroz, M.C., Stamelou, M., Bhatia, K.P. & Burn, D.J. The expanding universe of disorders of the basal ganglia. *Lancet* **384**, 523–531 (2014).
48. Saunders, A., Huang, K.W. & Sabatini, B.L. Globus pallidus externus neurons expressing parvalbumin interconnect the subthalamic nucleus and striatal interneurons. *PLoS One* **11**, e0149798 (2016).
49. Knowland, D. *et al.* Distinct ventral pallidal neural populations mediate separate symptoms of depression. *Cell* **170**, 284–297.e18 (2017).
50. Ye, L. *et al.* Wiring and molecular features of prefrontal ensembles representing distinct experiences. *Cell* **165**, 1776–1788 (2016).
51. Economo, M.N. *et al.* A platform for brain-wide imaging and reconstruction of individual neurons. *Elife* **5**, e10566 (2016).
52. Luo, L., Callaway, E.M. & Svoboda, K. Genetic dissection of neural circuits: a decade of progress. *Neuron* **98**, 256–281 (2018).
53. Chen, K.H., Boettiger, A.N., Moffitt, J.R., Wang, S. & Zhuang, X. Spatially resolved, highly multiplexed RNA profiling in single cells. *Science* **348**, aaa6090 (2015).
54. Beliveau, B.J. *et al.* Single-molecule super-resolution imaging of chromosomes and in situ haplotype visualization using Oligopaint FISH probes. *Nat. Commun.* **6**, 7147 (2015).
55. Spurr, A.R. A low-viscosity epoxy resin embedding medium for electron microscopy. *J. Ultrastruct. Res.* **26**, 31–43 (1969).

ONLINE METHODS

Protocols. Detailed protocols are available online (http://www.chunglabresources.com).

Molecular dynamics simulations. One hundred epoxide conformers in the fully ring-opened amine-reacted state were generated using the distance geometry method implemented in RDKit. After discarding conformers within 0.5-Å heavy atom r.m.s. deviation, the remaining structures were minimized with the MMFF94 force field[56,57]. Conformers were sorted by their MMFF energy and filtered again for uniqueness using a 1.0-Å heavy atom r.m.s. deviation cutoff on the postminimization geometries. Distances between the side-chain-mimicking nitrogen atoms were measured for the final minimized conformers.

A 227-residue, 3,567-atom EGFP (PDB ID: 4EUL) model was used for this study, where the chromophore was replaced with an alanine residue to simplify force field assignments. EGFP was protonated using the H++ webserver assuming a pH of 7.0, which yielded a net charge of −7. All simulations were carried out with the AMBER16 suite and with the AMBER tleap program for further protein preparation. A rectangular prism of water was added by adding at least 20 Å water buffer from the edge of the protein before NPT equilibration with periodic boundary conditions. A neutral simulation cell was obtained by adding Na$^+$ charges to this water cell, producing an initial simulation box roughly $89 \times 95 \times 100$ Å in size and containing 73,846 atoms. The AMBER ff14SB force field was used for the protein in MM simulations along with a TIP3P water force field and standard AMBER Na$^+$ force field parameters.

Before production molecular dynamics, equilibration was carried out as follows: (i) 1,000 constrained-protein (i.e., only solvent and ions are minimized while the protein is held fixed) and 2,000 free-protein minimization steps (i.e., everything in the system is minimized), (ii) 20 ps quick NVT heating to 50 K with a 0.5-fs time step, (iii) 20 ps quick NVT heating from 50 K to 300 K with a 0.5-fs time step, and (iv) 1.05 ns NPT equilibration ($P = 1$ bar, $T = 300$ K) with a 2-fs time step. Following this equilibration, 100 ns of NpT production dynamics was carried out. A Langevin thermostat was employed with a collision frequency of 5.0 ps^{-1} in all constant temperature equilibration or production, and a Berendsen barostat with a pressure relaxation time of 2.0 ps was employed for all constant pressure equilibration or production. A random seed was used to avoid synchronization artifacts in the case of Langevin dynamics constant temperature simulation. For all cases, at minimum the backbone (i.e., amide C or N and Cα atoms) of the protein were held fixed with a 500 kcal mol^{-1} Å^{-2} restraint to sample only configurational side chain dynamics of EGFP with the backbone held fixed to its orientation in the 1.35-Å resolution crystal structure[58]. In all cases, the SHAKE algorithm[59] (i.e., fixed X–H bonds) was employed to enable longer, 2-fs time steps, but shorter time steps were used during equilibration to avoid bubble formation during box size adjustment. For the long-range electrostatics, the particle mesh Ewald method was used with a 10-Å electrostatic cutoff.

Surface exposed residues were defined based on consensus of two metrics over the course of the entire 100-ns trajectory, as judged by analysis on 50,000 evenly spaced frames. The following metrics were employed. (1) A residue was considered buried if its side chain atom (lysine N, cysteine S, tyrosine O, histidine either N) had less than 2.5 Å^2 exposure to solvent. The surface was calculated using a 1.4-Å-radius probe with an in-house Python script that used the PyMOL dot_solvent built-in command. (2) The full residue's contribution to the total protein solvent-exposed surface area (SASA) was computed using the cpptraj utility in the AMBER suite over the trajectory, and the average, maximum and minimum contribution to SASA was retained. A buried residue based on the AMBER estimation will have a negative SASA. Residues that were deemed exposed in <10% of frames based on criterion 1 and had negative average or low maximum contributions to SASA were deemed buried for this analysis. This assignment of buried versus exposed was also verified by visual inspection. From 39 candidate epoxide-functionalization sites (i.e., lysine, cysteine, histidine and serine residues), 8 residues were judged to be buried (C48, C68, Y72, K83, Y90, Y104, H179 and H197) whereas the remaining 31 residues were deemed surface exposed (K3, H25, K26, Y39, K41, K45, K52, H75, K77, K79, K99, K105, K111, K124, K129, H137, K138, Y141, Y143, H146, Y149, K154, K156, K160, K164, H167, Y180, Y198, K207, K212 and H215). The trajectory from production dynamics was analyzed by computing all possible side chain–side chain distances on the surface-exposed, candidate epoxide functionalization sites of EGFP using a combination of the cpptraj utility in AMBER and our own in-house Python code. Analysis of minimum, maximum and average pairwise distances between the functional groups of only surface-exposed residues was carried out with in-house Python code and used to generate the histogram featured in the main text.

Recombinant GFP expression and purification. EGFP plasmid (Champion pET SUMO Expression System, Thermo Fisher) was transformed into BL21 *E. coli* competent cells and amplified in 1 L Terrific Broth (overnight, 37 °C) to an OD$_{600}$ of 0.5–0.6. EGFP expression was induced by adding IPTG (1 mM final concentration; overnight, 37 °C). The culture was pelleted and resuspended in lysis buffer (50 mM Tris-HCl, pH 7.5, 150 mM NaCl, 10 mM imidazole) and lysed by sonication followed by centrifugation at 31,400g (20 min, 4 °C). EGFP was purified with an Ni-NTA column with a 50-mL wash (50 mM Tris-HCl, pH 7.5, 150 mM NaCl, 25 mM imidazole) and eluted (50 mM Tris-HCl, pH 7.5, 150 mM NaCl, 500 mM imidazole). EGFP was further purified by size-exclusion gel chromatography using FPLC twice, first to remove imidazole and then to remove cleaved SUMO protein.

Preparation of epoxide solution. Glycidyl methyl ether (GME) was purchased from Sigma-Aldrich (cat no. 454680). The polyepoxide resins of ethylene glycol diglycidyl ether (EGDGE, product name EGDGE), 1,4-butanediol diglycidyl ether (1,4-BDE, product name GE21), dipropylene glycol diglycidyl ether (DGDE, product name GE23), polyglycerol 3-polyglycidyl ether (P3PE, product name GE38) and pentaerythritol polyglycidyl ether (PEGE, product name GE40) were provided by CVC Thermoset Specialties of Emerald Performance Materials. The resin of glycerol triglycidyl ether (TGE, product name EX-313) was provided by Nagase America Corporation. The resins were weighed and dissolved in an aqueous solution and then thoroughly vortexed for 1 min. The resulting suspension was centrifuged for 5 min at 7,200g. and the supernatant was collected. This procedure was repeated until the supernatant became fully transparent. Most of the GE38 resin is water insoluble. From BSA amine reaction assay, we found that the amine reactivity of supernatant of 1% (w/v) GE38 at 37 °C in pH 10, 0.1 M sodium carbonate buffer is comparable to that of 0.475% (w/v) PFA in pH 7.4, 0.1 M sodium phosphate buffer with 10 mM NaCl at room temperature (RT). We prepared the following solutions using the supernatant of 10 or 20% (w/v) GE38 resin:

SHIELD perfusion solution: ice-cold PBS containing 4% (w/v) PFA and GE38 supernatant.

SHIELD-OFF solution: ice-cold PBS containing GE38 supernatant

SHIELD-ON solution: 0.1 M sodium carbonate buffer at pH 10, prewarmed to 37 °C

SHIELD whole organ processing protocol. *Fixation.* Mice were transcardially perfused with ice-cold PBS and then with the SHIELD perfusion solution. Dissected brains or organs were incubated in the same perfusion solution at 4 °C for 48 h. Tissues were then transferred to the SHIELD-OFF solution and incubated at 4 °C for 24 h. In the case of brain hemisphere clearing, an intact whole brain was split into hemispheres before being incubated in the SHIELD-OFF solution. Following the SHIELD-OFF step, the organs were placed in the SHIELD-ON solution and incubated at 37 °C for 24 h. Alternatively, if the tissues had been previously fixed with PFA, samples were washed in PBS with 0.02% sodium azide at RT for at least 24 h, and then incubated in the SHIELD-OFF solution for 3 d (in case of mouse brain hemispheres) at 4 °C. The final SHIELD-ON step was the same as the procedure for perfused tissue described above.

Delipidation. SHIELD-fixed organs were cleared passively for a couple of weeks (10–14 d at 45 °C for a mouse brain hemisphere) in SDS-based clearing buffer (300 mM SDS, 10 mM sodium borate, 100 mM sodium sulfite, pH 9.0) or rapidly cleared (<3 d for a mouse brain hemisphere) using stochastic electrotransport (SmartClear Pro, LifeCanvas Technologies).

Optical clearing. Delipidated tissues were incubated in Protos-based immersion media (125 g iohexol, 3 g diatrizoic acid, 5 g *N*-methyl-D-glucamine dissolved in 100 mL deionized (DI) water with the refractive index adjusted to 1.458 by adding DI water, or 50 g diatrizoic acid, 40 g *N*-methyl-D-glucamine, 55 g iodixanol in 100 mL DI water with the refractive index adjusted to 1.458

by adding DI water) until the tissue became transparent without any visible haze at the tissue–medium interface.

GFP fluorescence retention screen. An aliquot of GFP at a concentration of 0.5 mg/mL was reacted in either the supernatant of 1% (v/v) epoxide suspended in 0.1 M sodium carbonate buffer at pH 10 or aldehyde fixative in PBS for 12 h at 37 °C. Excess cross-linker was removed by centrifugal filtration (10 kDa MWCO, Amicon), and the GFP was reconstituted in 0.1 M HEPES buffer at pH 7.5. Cross-linked GFP (0.1 mg/mL) or GFP in additive solution (0.1 mg/mL in 0.1 M of xylitol, sorbitol, trimethylamine N-oxide or trehalose) was exposed to 90 °C for 10 min or incubated in 70% (v/v) methanol for 1 h. Fluorescence was quantified with a UV-visible spectrometer (EnSpire Multimode Plate Reader 2300, PerkinElmer).

Physiochemical characterization of GFP. An aliquot of the cross-linked GFP solution was obtained using the same protocol as for the fluorescence retention screen. Differential scanning calorimetry (MicroCal VP-DSC, Malvern Instruments) was performed on the cross-linked GFP solution at a heating rate of 1.5 °C/min (2 mg/mL, 0.1 M HEPES, pH 7.5). Circular dichroism spectra (J-1500 CD Spectrometer, JASCO) were collected from the cross-linked GFP solution (0.1 mg/mL in 10 mM sodium carbonate buffer at pH 8). GFP refolding experiments were performed according to previously established protocols. Briefly, 50 µL of GFP (1 mg/mL, 50 mM HEPES, pH 7.5) was combined with 50 µL dithiothreitol solution (2 mM dithiothreitol, 50 mM HEPES, pH 7.5) and incubated for 5 min. Then 100 µL of 0.1 M HCl was added and the mixture was incubated for an additional 5 min. Refolding was initiated by diluting the GFP mixture in TNG (0.1 M Tris, pH 7.5, 150 mM NaCl, 10% [w/v] glycerol) at a ratio of 1:10. Fluorescence recovery was measured using a UV-visible spectrometer (EnSpire Multimode Plate Reader 2300, PerkinElmer).

Amine reactivity quantification. o-Phthaldialdehyde (OPA) reagent (Fluoraldehyde, Thermo Fisher) was used to quantify the degree of epoxidation of amine residues on GFP and bovine serum albumin (BSA) proteins. BSA (1 mg/mL) was reacted with the supernatants of 1% (v/v) fixative for 12 h at 37 °C (0.1 M carbonate buffer at pH 10 for epoxides, PBS at pH 7.4 for aldehydes). After removing excess reactants by filter centrifugation (3× PBS with the Amicon Ultra 30K NMWL, Millipore), 10 µL of reacted BSA (1 mg/mL reacted BSA in PBS) was incubated with 200 µL OPA and measured within 5 min (Ex350, Em450). To determine the SWITCH on/off condition of P3PE, 100 mg/mL BSA was incubated with the supernatant of 10% (w/v) P3PE for 1 d in either 0.1 M sodium phosphate dibasic and 10 mM NaCl solution buffered at pH 7.4 at 4 °C or 0.1 M sodium carbonate solution buffered at pH 10 at either 4 °C or 37 °C. Aliquots were removed and diluted by 20-fold in the same pH buffers to be measured within the linear response of the OPA reagent, and the degree of epoxidation was quantified with OPA without further purification. Measured values were normalized to the values obtained from BSA stock solutions at various concentrations, immediately after the addition of cross-linkers.

Nucleic acid reactivity. $(dA)_{15}$ and $(dC)_{15}$ single-strand DNA oligonucleotides synthesized by IDT were used for testing nucleic acid reactivity to epoxides. Due to the difficulty in synthesis of polydeoxyguanine, we excluded the $(dG)_{15}$ oligonucleotide. We also excluded polydeoxythymine due to its weak nucleophilicity, yielding minimal cross-linking. Oligonucleotides at 250 µM were reacted with 1% (w/v) GME or the supernatant of 5% (w/v) P3PE in 0.1 M sodium carbonate buffer (pH 10) for 15 h (GME) or 2 d (P3PE) at 37 °C. The resulting reaction mixtures were subject to the standard ethanol precipitation to remove salts and unreacted epoxides and their molecular weight changes were determined by the MALDI mass spectrometry.

Mass spectrometry. Cross-linked BSA (1 mg/mL) was concentrated 40-fold (Amicon, 30 kDa MWCO, Millipore). An aliquot of 1 µL of cross-linked BSA was mixed with 4 µL of 10 mg/mL sinapinic acid matrix solution in 50% acetonitrile, 0.1% trifluoroacetic acid and spotted on a MALDI sample plate. An aliquot of 1 µL of cross-linked oligonucleotide after ethanol precipitation and tenfold dilution with Millipore water was mixed with 1 µL of the

9:1 mixture of 50 mg/mL 3-hydroxypicolinic acid in 50% acetonitrile and 50 mg/mL diammonium hydrogen citrate in Millipore water as a matrix. MALDI mass spectra were acquired by a Bruker MicroFlex MALDI-TOF mass spectrometer.

Mice. Young adult (2–4 months; median age 3 months) C57BL/6 mice were housed in a 12 h light/dark cycle with unrestricted access to food and water. All experimental protocols were approved by the MIT Institutional Animal Care and Use Committee and the Division of Comparative Medicine and were in accordance with guidelines from the National Institute of Health. All experiments using mice were conducted in strict adherence to the ethical regulations of MIT Institutional Animal Care and Use Committee and the Division of Comparative Medicine. The following transgenic lines were used for this study: Thy1::GFP M-line, Thy1::YFP H-line, ChAT[BAC]-eGFP (Jackson stock no. 007902), PV-Cre loxP-tdTomato (Jackson stock no. 017320 and 007914) and Fos-CreER[T2] DIO-tdTomato (Jackson stock no. 021882, 007914). For the footshock experiment, mice were habituated in the fear-conditioning box for 10 min, followed by two sequential 5 s of 0.6-mA electric shocks at a 30-min interval. Five minutes after the second electric shock, mice were perfused.

Fluorescent protein tissue epoxide screen. The 100-µm coronal slices were obtained from the 4% (w/v) PFA-perfused Thy1::GFP M-line mouse. The slices were incubated in 1% fixative solution (1% w/v GA in PBS; the supernatant of 1% w/v epoxide in 0.1 M sodium bicarbonate buffer pH 9.5) for 6 h at 37 °C and washed with an excess of PBS containing 0.1% (w/v) Triton-X 100 (PBST). Additional 100-µm slices were obtained from CLARITY-embedded brains[50]. Processed slices were heated to 70 °C in PBS for 24 h. The entire coronal slice was imaged before (after PFA fixation only) and after thermal or chemical treatment (after tissue processing). Fluorescence retention was calculated with ImageJ by normalizing the mean intensity signal from the same five regions before and after treatment following background subtraction (N = 3 tissues samples). Tissue slices with neurons expressing different fluorescent proteins were similarly processed and analyzed.

Fluorescence retention after exposure to chemical conditions was quantified with Thy1::GFP M-line 100-µm coronal slices. Slices were processed with 80% (v/v) methanol in DI water (RT, 4 d), 100% THF (RT, 12 h), uDISCO (50%, 80%, 95%, 100% (v/v) *tert*-butanol dehydration (37 °C, 15 min each step) and BABB-D4 (benzyl alcohol, benzyl benzoate and diphenyl ether at a ratio of 4:8:1) for 1 h), CUBIC-L (5% (w/v) Triton X-100, 5% (w/v) N-butyldiethanolamine; 37 °C, 5 d) and SDS clearing buffer (200 mM SDS, 100 mM sodium sulfite and 10 mM sodium borate pH 9.5; 37 °C or 56 °C, 12 h). Note that thereafter when we refer the SDS clearing buffer, it contains either 200 or 300 mM SDS, 100 mM sodium sulfite and 10 mM sodium borate at pH 9.0 or 9.5 (indicated in each section).

Preparation of PFA, GA, PACT and iDISCO+ tissues. For PFA tissue preparation, mice were intracardially perfused with ice-cold PBS, with ice-cold 4% (w/v) PFA in PBS (5 mL/min), and then dissected tissues were postfixed in PBS with 4% (w/v) PFA at 4 °C for 48 h. Fixed tissues were washed with PBS with 0.02% sodium azide at room temperature overnight.

To prepare GA-processed mouse brains, ice-cold 4% (w/v) PFA, 1% glutaraldehyde (16310, Electron Microscopy Sciences) in PBS (5 mL/min) was prepared (glutaraldehyde was added after the PFA-containing PBS solution cooled to 4 °C) and then used for perfusing the mouse after ice-cold PBS perfusion. After 2 d of postfixation in the perfusion solution containing fixatives, brains were split into hemispheres and then washed with PBS containing 0.1% Triton-X100 and 0.02% sodium azide at room temperature overnight. Tissues were inactivated in PBS with 1% (w/v) acetamide and 1% (w/v) glycine at 37 °C overnight and then washed with PBS with 0.02% sodium azide at room temperature overnight.

PACT tissue preparation was done based on the previous publication[60]. Briefly, PFA brains postfixed at 4 °C for 24 h were split into hemispheres and then moved to ice-cold hydrogel monomer solution (4% acrylamide and 0.25% azo-initiator VA-044 in PBS), then incubated at 4 °C for 24 h. Brain in 10 mL of the hydrogel monomer solution was gelated under nitrogen gas purging (10 p.s.i.) at 37 °C for 2 h. Excess hydrogels were washed with PBS with 0.02% sodium azide at room temperature overnight.

CLARITY tissues for immunoreactivity (**Fig. 2i,j**), autofluorescence (**Fig. 2g**) and tissue rigidity (**Fig. 3g,h**) comparisons were prepared based on Kim *et al.*[28] with some modifications. Hydrogel monomer solution was made with 4% (w/v) acrylamide (A3553, Sigma), 0.25% (w/v) VA-044 (Wako Chemicals), 4% (w/v) PFA (15714-S, Electron Microscopy Sciences) in PBS (70011-044; Invitrogen). After perfusion with ice-cold PBS, mice were perfused with 20 mL of the hydrogel monomer solution, followed by incubation in the monomer solution at 4 °C for 72 h. The brains were split into hemispheres and were moved to 10 mL of fresh hydrogel monomer solution. Samples were gelated at 37 °C for 2 h with nitrogen gas purging (10 p.s.i.). After retrieval from the polymerized solution, gel pieces on the hemisphere surface were gently removed and the hemispheres were washed with PBS with 0.02% sodium azide at room temperature overnight. For EDC-CLARITY experiments, CLARITY-processed brains were sliced into 100-μm sections and then postfixed in EDC-based solution (0.1 M 1-ethyl-3-(3-dimethylaminopropyl)-carbodiimide, 0.1 M 5-ethylthio-1H-tetrazole, 0.1 M methylimidizole pH 8.5) overnight at 37 °C (ref. 12) and used for oligo-dT staining. For tissue integrity comparisons (**Fig. 3a–f**), CLARITY tissue preparation was based on that of Ye *et al.*[50] without modification.

iDISCO+ tissue preparation for tissue antigenicity, autofluorescence measurement and rigidity comparison was performed by following the original iDISCO+ protocol[61] with minor modifications. PFA tissues (see above) postfixed at 4 °C 24 h were washed in PBS with 0.02% sodium azide at room temperature overnight. After cutting into hemispheres, tissues were dehydrated sequentially with 20%, 40%, 60% and 80% MeOH for 1 h each at RT, followed by 100% MeOH twice for 1 h each. Tissues were chilled at 4 °C and bleached with prechilled 5% H_2O_2 (1:5 dilution of 30% H_2O_2 with MeOH) at 4 °C overnight. After briefly washing with 100% MeOH twice, tissues were rehydrated sequentially in 80%, 60%, 40% and 20% MeOH for 1 h each at RT, followed by PBS with 0.02% sodium azide for 1 h at RT. At this point, 100-μm slices or 1-mm sagittal blocks were prepared by a vibratome and further processed for each experiment (see "Tissue antigenicity test" and "Tissue rigidity comparison"). For tissue integrity and size comparison measurements, we followed the most recent iDISCO+ protocol from the iDISCO website (https://idisco-dotinfo.files.wordpress.com/2015/04/whole-mount-staining-bench-protocol-methanol-dec-2016.pdf).

Virus injection. Mice were anesthetized using 3% isoflurane with oxygen (1 L/min). After loss of the toe-pinch reflex, the skull was secured onto a stereotaxic (Kopf), and 500 nL of RV-mOrange-PSD95-EGFP was injected bilaterally into the dentate gyrus (−3.5 mm, ±2.5 mm, −2.8 mm for the anterior-posterior (AP), medio-lateral (ML) and dorso-ventral (DV) axes from bregma). At 6 d after injection, the mice were killed and PFA-processed.

Autofluorescence analysis. C57BL/6 mice were perfused and then prepared according to the standard protocols of each tissue-processing method described above. Fixed samples were then sliced into 100-μm sections using a vibratome. Tissues postfixed with glutaraldehyde at 37 °C were prepared using the postfixation protocol described above. Tissues were cleared in either the 200 mM SDS buffer (pH 9.5, 37 °C, 3 d; GA, CLARITY, SHIELD), 8% SDS buffer (pH 7.4, 37 °C, 3 d; PACT), or 67% dichloromethane, 33% methanol (3 h, RT for 100-μm slices; iDISCO+). After SDS-based buffer clearing, tissues were extensively washed with PBST overnight before imaging. Uncleared PFA tissues and cleared GA (both fixed at 4 °C and 37 °C), PACT, CLARITY, SHIELD and iDISCO+ tissues were immersed in optical clearing media (PACT: RIMS[60], iDISCO+: dibenzyl ether (DBE), others: Protos-based immersion medium with 50 g of diatrizoic acid) for imaging. The samples were imaged with four commonly used excitation wavelengths—405, 488, 561 and 630 nm—with emission detection ranges of ~60 nm (+5 nm to ~+65 nm from the excitation wavelength) to measure background autofluorescence. Images were acquired from similar regions of brain with similar coordinates and at least three independently perfused and processed mice brains were used for the experiments. 100-μm slices of RV mOrange-expressing tissue (see "Virus injection") were fixed with GA or SHIELD according to the slice fixation protocol and subjected to confocal microscope imaging (see **Supplementary Table 3** for imaging conditions).

Protein loss quantification. Coronal brain blocks 1 mm thick (PFA control, GA-processed or SHIELD-processed) were incubated in 1 mL of SDS clearing solution (200 mM SDS, pH 9.0) for 12 h at 70 °C. The protein content of the supernatant was quantified using a Bio-Rad DC protein assay kit, following the instructions in the manufacturer's manual.

Tissue antigenicity test. GA, PACT, CLARITY and SHIELD-processed mice brain sections with 100 μm thickness (see "Preparation of PFA, GA, PACT and iDISCO+ tissues") were cleared at 37 °C for 3 h with either 8% SDS buffer at pH 7.4 (PACT) or 200 mM SDS buffer at pH 9.5 (GA, CLARITY and SHIELD). Cleared sections were thoroughly washed with PBS with 1% Triton-X 100 by multiple buffer exchanges, followed by overnight incubation at RT, and then used for immunostaining. Uncleared PFA and cleared GA, PACT, CLARITY and SHIELD-processed mouse brain sections were incubated in PBST with 2% normal donkey serum (NDS) at RT for 1 h for blocking, followed by incubation with primary antibodies [rabbit anti-FoxP2 (ab16046, Abcam, MA), rabbit anti-calretinin (ab702, Abcam, MA), rabbit anti-parvalbumin (PV27, SWANT, Switzerland), rabbit anti-NeuN (2430S, Cell Signaling Technology), mouse anti-GFAP (3670S, Cell Signaling Technology), rabbit anti-iba1 (019-19741, Wako Chemicals, Japan), rat anti-MBP (ab7349, Abcam, MA), mouse anti-NF-H (2836S, Cell Signaling Technology)] with a 1:300 dilution factor (1 μL in 300 μL of PBST with 2% NDS) at RT overnight. For iDISCO+ slices, the original protocol[61] was employed with permeabilization, blocking and primary staining buffers as described in the paper, with a 1:300 dilution factor for primary antibody incubation (see "Preparation of PFA, GA, PACT and iDISCO+ tissues"). After washing with PBST with 2% NDS or iDISCO+ washing buffers for at least 8 h, the sections were incubated in PBST with 2% NDS with corresponding secondary antibodies (anti-rabbit, 111-607-008; anti-mouse IgG1, 115-607-185; anti-rat, 112-607-008; Jackson Immunoresearch; 1 μL in 300 μL of PBST with 2% NDS, or iDISCO+ secondary staining buffer) overnight at RT. Washing was performed in PBST with 2% NDS or iDISCO+ washing buffers at RT for at least 8 h, followed by PBST washing for 1 h. The sections were then imaged in PBST using a confocal microscope. For delipidation, the iDISCO+ sections were dehydrated in 20%, 40%, 60%, 80% and 100% MeOH for 5 min each, briefly cleared in 67% dichloromethane, 33% MeOH for 15 min, briefly washed in 100% dichloromethane, and then rehydrated in 67% dichloromethane, 33% MeOH, 100%, 80%, 60%, 40%, 20% MeOH, PBS and PBST for 5 min each. All images were acquired at the very surface of tissue sections, where the background signal induced by light scattering disappeared. Similar brain regions with similar coronal coordinates were chosen to allow pair-wise comparisons among different tissues (PFA control, GA, PACT, CLARITY, SHIELD and iDISCO+ processed). To quantify the SNRs of antibody staining, three sections from each group were prepared, stained and imaged as described above. Regions of interest for signal and background measurements were manually segmented, and their mean intensities were analyzed using ImageJ software.

For the antibody compatibility test in **Supplementary Figure 2a,e,g,h**, uncleared PFA control, GA or SHIELD-fixed mouse brain sections at 200 μm thickness were incubated in PBST with primary antibodies (1 μg in 200 μL of PBST) at RT overnight. When the concentration of antibody was unknown, 1 μL of antibody was used. After washing with PBST for several hours, sections were incubated in PBST with corresponding secondary antibodies (2 μg in 200 μL of PBST) at RT overnight. Sections were then imaged in PBST using a confocal microscope after washing in PBST at RT for at least 8 h. To avoid light scattering caused by tissue opacity, all images were acquired at the very surface of tissue sections, within the top 10 μm. Similar brain regions within similar coronal coordinates were chosen to allow pair-wise comparisons among different tissues (PFA control, GA, SHIELD-processed). To quantify the SNRs of antibody staining, four sections from each group were prepared, stained and imaged as described above. Image analysis was performed as described in the paragraph above.

Multiround immunostaining. SHIELD-processed coronal slices obtained from H-line mice at 100 μm thickness were stained with primary antibodies (5 μg per antibody) preincubated with dye-conjugated Fc-specific Fab fragments (3:1 molar ratio between the Fab fragment and the primary antibody, Jackson Immunoresearch) for 12 h at 4 °C in PBST. Following imaging, the

slices were incubated in the destaining buffer (7 mM SDS, 0.5 M Tris-HCl, 1% (w/v) 2-mercaptoethanol, pH 6.8) for 18 h at 37 °C to remove bound antibodies. Subsequent rounds of immunostaining were performed similarly.

Fluorescence in situ hybridization (FISH)–hybridization chain reaction (HCR). To demonstrate the versatile applicability of SHIELD tissue for various FISH experiments, a series of oligonucleotide probes with different lengths of antisense probe sequences were employed. DNA oligonucleotides with 18- to 22-nt, 35-nt and 50-nt antisense sequences carrying B1, B3 and B5 initiator sequences flanking the 5′ or 3′ ends for 18- to 22-nt and 35-nt probes and flanking both ends for 50-nt probes were synthesized by IDT (Coralville, IA) and used without further purification. Dye-conjugated hairpin probe sets (B1-Alexa Fluor 647, B3-Alexa Fluor 488 and B5-Alexa Fluor 546) were purchased from Molecular Instruments (Pasadena, CA) or prepared in-house using the standard NHS-ester coupling reaction scheme (B1-Cy5)[62].

Probe sequences for somatostatin (B5-SST), neuropeptide Y (B1-NPY), YFP (B1-YFP) and GAD1 (B1-GAD1, 22 nt) were obtained as previously described[12,62–64]. For 35-nt probes, we tiled 35-nt *Gad1* and *Fos* probes along the coding regions of the target genes and selected probe sequences to be 45–60% GC and melting temperatures to be <80 °C. *vGluT1* and *vGluT2* 35-nt probes were designed by OligoArray under the guidance of the previous publication[65]. The 3′ end of the 35-nt probe sequences was appended to a 4-nt ATAT linker followed by the B1I2, B3I2 or B5I2 HCR initiator sequences.

Using 100- or 200-μm SHIELD tissues cleared at 37 °C for 12 h using 200 mM SDS buffer at pH 9.5, initial transcript-targeting probe hybridization was performed overnight (37 °C, 15–16 h) in hybridization buffer (30% (v/v) formamide for 18- to 22-nt probes, 30–40% (v/v) formamide for 35-nt probes, and 50% (v/v) formamide for 50-nt probes, in 2× SSC with 10% (w/v) dextran sulfate with an average MW of 500 kDa (Sigma D8906) and 1 mg/mL salmon sperm DNA (Sigma D7656, using 10 mg/mL stock, 10 min boiling for denaturation and 10 min snap-cooling in ice before use) at probe concentrations of 1 nM for 18- to 22-nt probes and 2 nM for 35- and 50-nt probes. Once hybridization was finished, stringent washing was performed using three rounds of formamide wash (30% (v/v) formamide for 18- to 22-nt probes or 50% (v/v) formamide for 35- and 50-nt probes in 2× SSCT (0.1% (v/v) Triton X-100), for 1 h each wash at RT for 18- to 22-nt and 35-nt probes and at 37 °C for 50-nt probes), followed by two rounds of 2× SSCT washing at RT for 1 h each. Tissue slices were then placed in amplification buffer (2× SSC, 10% (w/v) dextran sulfate) and equilibrated for 30 min before the addition of appropriate hairpin sets. Before incubation, hairpins were heated to 95 °C for 90 s, then snap-cooled on ice for 30 min. HCR amplification was performed overnight at RT using hairpin concentrations of 120–240 nM in the amplification buffer. After HCR was finished, the samples were washed with three rounds of 2× SSCT, 1 h each at RT, and subjected to confocal imaging.

For (dT)$_{50}$-Cy3 oligonucleotide FISH performed to compare the retention of mRNA among PFA, EDC-CLARITY, GA and SHIELD-processed tissues, 100-μm-thickness tissues cleared at 37 °C for 1 d were hybridized as described before[12] and imaged with a confocal microscope. For the whole-organ-level transcript preservation test, a mouse hemisphere was processed by SHIELD epoxidation with a perfusion protocol, followed by stochastic electrotransport clearing at 37 °C for 8 d. The cleared hemisphere brain was washed in PBST for 1 d at 37 °C with multiple solution changes. Afterwards, a 1 mm slice was obtained by cutting at the central coordinate using a vibratome and hybridized for 2 d at 37 °C as described before[12], then washed in 2× SSCT, 15% (v/v) formamide at RT for 1 d and 2× SSCT for 3 h at RT. The sample was immersed in Protos-based immersion medium until optically cleared and imaged using a 25×, 0.95 NA water objective. The uniformity of mRNA preservation across the tissue area was determined by oligo-dT staining targeting against poly(A) tails of mRNA molecules.

Structural integrity and tissue size comparison. 1-mm-thick tissue blocks from four different coronal coordinates were cut from hemispheres that had been fixed and/or embedded for PACT, CLARITY, iDISCO+ or SHIELD processing. The surfaces of 1-mm-thick blocks were imaged for autofluorescence signal to record their initial tissue structures. Afterwards the tissue blocks were cleared according to corresponding clearing conditions of each technique[50,60]. For SHIELD tissue blocks, 37 °C 300 mM SDS buffer was used.

In case of iDISCO+ blocks, the most updated iDISCO+ protocol from the iDISCO website (https://idiscodotinfo.files.wordpress.com/2015/04/whole-mount-staining-bench-protocol-methanol-dec-2016.pdf) was used for clearing. To mimic hemisphere tissue clearing condition, 1-mm-thick tissues were delipidated for three times the duration necessary to render the blocks evenly translucent. The delipidated samples were optically cleared and mounted in a manner that prevents any physical compression of the tissue, and autofluorescence and YFP signals of the tissue blocks were imaged. Changes in structural integrity were assessed by calculating the change in ratio between medio-lateral and dorso-ventral lengths of the individual tissue blocks. Changes in the means of medio-lateral and dorso-ventral lengths were used to calculate the size change of the individual tissue blocks. Hemispheres in **Supplementary Video 2** were cleared with the same condition as for the 1-mm-thick tissue, while the PACT hemisphere was cleared for 6 d and the SHIELD hemisphere was cleared with a SmartClear II Pro (Life Canvas Technologies, MA) at 42 °C for 5 d.

Tissue rigidity comparison. Brain hemispheres of C57BL/6 mice were prepared with the standard protocol for each tissue processing method by perfusion (see "Autofluorescence analysis"). Sagittal sections at the most medial coordinate with 1 mm thickness were acquired by cutting on a vibratome. Tissues were cleared using either 200 mM SDS buffer (pH 9.5, 45 °C: PFA, 1 d; CLARITY, 3 d; SHIELD 2.5 d), 8% SDS buffer (pH 7.4, 45 °C, 1d; PACT), or 67% dichloromethane/33% methanol (3 h, RT; iDISCO+). After SDS clearing, tissues were washed with 1X PBST (0.1% v/v Triton X-100) for 1 d. iDISCO+ tissues were washed with 100% DCM for 20 minutes twice, then incubated in DBE. Tissues were balanced on a lab brush to measure the relative curvature caused by gravity. The curvature was extracted from a tissue photo by interpolating the centerline of the tissue using graphical user interface–based Matlab code, img2curve.m from mathworks.com. At least three independently prepared sections were employed to obtain the mean curvature value for each tissue processing method.

Rapid SPIM imaging and automatic atlas alignment. SHIELD brain hemispheres were imaged using an axially swept[66,67] light-sheet microscope (SmartSPIM, Lifecanvas Technologies, MA) equipped with a 2.6×, NA 0.2 detection objective (uniform axial resolution ~4 μm). Postprocessed images were downsampled to $25 \times 25 \times 25$ μm voxel size and automatically aligned to annotated autofluorescence atlas from Allen Brain Institute (version 3)[68] by linear and nonlinear image transformation processes.

SHIELD processing of human tissues. Human brain tissues were obtained from the Massachusetts General Hospital brain bank. The 2-mm-thick coronal slabs were incubated in the supernatant of 10% (w/v) P3PE solution in PBS for 2 d at RT, then were incubated in the supernatant of 10% (w/v) P3PE solution in 0.1 M sodium carbonate buffer at pH 10 at 37 °C for 3 h. Following fixation, human tissues were cleared passively via incubation in the same SDS-based clearing solution (200 mM SDS, pH 9.5) at 80 °C until transparent. Optical clearing of human tissues was done with Protos-based immersion medium.

Human tissue staining. For **Figure 4c**, tissues were stained using lectin 594 and syto16 nuclear dye at 37 °C. For antigenicity testing for **Figure 4**, 100-μm slices were generated from a piece of human brain tissue with a vibratome and SHIELD-processed as described above. The tissues were cleared at 37 °C for 1 d and thoroughly washed in PBST for 1 d. Antigen retrieval and anti-autofluorescence treatments were performed by incubation in 10 mM sodium citrate buffer at pH 6 with 0.05% (v/v) Tween 20 for 3 h at 80 °C for antigen retrieval, followed by incubation in 50 mM ammonium acetate and 100 mM copper sulfate solution overnight at RT for reduction of autofluorescence[69]. After thorough washing in PBST, tissues were incubated with rabbit anti-parvalbumin (ab11427, Abcam, MA), rabbit anti-calretinin (ab702, Abcam, MA), rat anti-MBP (ab7349, Abcam, MA), mouse anti-NFL (846002, BioLegend), chicken anti-GFAP (GFAP, Aves), rabbit anti-NPY (30914, Abcam, MA), rabbit anti-Iba1 (019-19741, Wako Chemicals, Japan), rabbit anti-MMP-13 (39012, Abcam, MA), mouse anti-SMI312 (24574, Abcam, MA), rabbit anti-calbindin (ab11426, Abcam, MA), chicken anti-TH (TYH, Aves) or mouse anti-TPH2 (PA1-778, Invitrogen) in PBST overnight at RT using 1:300 dilution factors for all but NFL (1:150). After the primary antibody incubation, tissues were

washed in PBST for 3 h at RT, and incubated in dye-conjugated secondary antibodies (Abcam, MA) for 3 h at RT using 1:300 dilution factors. Tissues were then washed in PBST for 3 h at RT and mounted in Protos-based immersion medium. Once the tissues were optically cleared, the samples were imaged with Leica confocal microscope using 10× 0.3 NA, 20× 0.5 NA or 25× 0.95 NA water immersion objectives.

For 1-mm-thick human brain tissue used for volumetric immunostaining, a piece of human cortical section (typically 1 cm × 1 cm × 1 mm) was incubated in the supernatant of 10% (w/v) P3PE solution in PBS for 1.5 d at 4 °C. The tissue was thermally equilibrated to RT for ~15 min, followed by incubation in the supernatant of 1% (w/v) P3PE solution in 0.1 M sodium carbonate buffer at pH 10 at 37 °C for 1 d. Following fixation, tissues were washed three times with PBS for 1 h at RT, and then were passively cleared in the SDS clearing solution (200 mM SDS, pH 9.5) at 80 °C overnight. Cleared tissues were extensively washed with PBST and the solution was exchanged four or five times during the course of the day, followed by overnight incubation. Antigen retrieval was performed as previously described, but no copper sulfate treatment was conducted. For antibody staining, a piece of 1-mm-thick tissue was cut to a size of 2 mm × 3 mm × 1 mm. The tissue was subjected to primary antibody staining using mouse anti-GFAP (3670S, Cell Signaling Technology) and rabbit anti-calretinin (ab702, Abcam, MA) in PBST at RT for 2 d using a 1:50 dilution factor (10 μL antibody solution in 500 μL PBST). Then the tissue was washed with PBST for 1 d with frequent solution exchanges, followed by overnight incubation. Secondary antibody staining was performed with Fab fragment dye conjugates with RRX (anti-Rb, 111-297-008, Jackson ImmunoResearch) and Alexa 647 (anti-mouse IgG1, 115-607-185, Jackson ImmunoResearch) from Jackson ImmunoResearch in PBST at RT for 2 d using a 1:50 dilution factor. After PBST washing for 1 d, the tissue was immersed in Protos-based immersion medium until optically cleared and imaged by a Leica confocal microscope with a 25×, 1.0 NA CLARITY objective immersed in RI-matching oil (RI = 1.458). A z-step size of 3 μm was used to image the tissue volume of, 443.29 μm × 443.29 μm × 1,017 μm.

Biopsy sample processing. Fresh mouse brains were dissected and placed in ice-cold PBS before core needle biopsy samples were prepared by piercing using an 18G blunt needle with a sharpened tip. Biopsies were incubated for 45 min in PFA (4% (w/v) in PBS) or in SHIELD perfusion solution, followed by 0.1 M sodium carbonate buffer at pH 10 for 30 min. All solutions were prewarmed and maintained at 37 °C during incubation. For tumor biopsy sampling, mouse kidney tissue harboring breast cancer metastasis was used. Human breast cancer cell line MDAMB231 was inoculated into immunodeficient NSG mice via left ventricle injection. Five weeks after injection, animals were perfused with ice-cold PBS, followed by 4% ice-cold PFA. Organs harboring metastasis were collected and put into long-term storage in 4% PFA in PBS at RT. SHIELD processing was performed in the same manner described above except that PFA was not included in the SHIELD perfusion solution because the kidney had been cured (>1 month) in 4% PFA in PBS at RT. 1-mm-square pole biopsies were prepared from a mouse kidney using a vibratome and a surgical knife.

Rapid clearing and staining of biopsy samples. Rapid clearing of fixed biopsy tissues was achieved with a modified SmartClear II Pro (Life Canvas Technologies) with an external 300 W electrophoresis PowerPac HC power supply from Bio-Rad to apply higher voltage (250V). To maintain the temperature below 70 °C, all insulation material in the SmartClear II Pro was removed and the device was operated in a cold room at 4 °C. Operational parameters for the SmartClear device were 4–6 V/mm for electric field strength, 0.1 r.p.m. for electric field rotation frequency and 70 °C for clearing temperature. 3% (w/v) SDS buffer titrated to 9.5 pH was used as the clearing buffer. The cleared biopsy tissues were stained using a custom device as described by Kim *et al.*[28]. Operational parameters were 8–10 V/mm for electric field strength, 0.1 r.p.m. for electric field rotation frequency and 30 °C for staining temperature. 20 mM Tris buffer titrated to pH 7.5 with 20% (w/v) D-sorbitol and 1% (w/v) BSA was used as the staining buffer. The samples were stained for 1 h with 5 μL of 10× concentrated lectin-594 (DL-1177, Vector Laboratories, CA) and 15 μL of rabbit anti-histone-H3 antibody (12230S, Cell Signaling Technology, MA) in 4 mL of staining buffer. 20 μL of anti-Ki-67 antibody (11882S, Cell Signaling Technology, MA) was used for labeling mouse kidney biopsy tissue.

SHIELD-MAP tissue processing protocol. SHIELD-processed mouse brain tissues were cleared with 300 mM SDS clearing buffer (pH 9.0) for 10 d at 37 °C (for a 1-mm-thick block) or at 45 °C (for a 3-mm-thick block or hemisphere) while shaking, then washed overnight at RT with PBS containing 1% (v/v) Triton-X100 and then with PBS. If necessary, cleared tissue was cut with a vibratome (VT1000S, Leica Biosystems, Germany). The tissue was then incubated in 4 °C monomer solution (30% [w/v] acrylamide [A3553, Sigma-Aldrich], 0.1% [w/v] bis-acrylamide [2% Bis solution, Bio-Rad, CA], 10% [w/v] sodium acrylate [408220-100G, Sigma-Aldrich] and 0.03% [w/v] VA-044 [Wako Chemicals, Japan]) in PBS. Monomer solution incubation was done for >8 h for 200-μm-thick sections, >1 d for 1-mm-thick blocks, or >2 d for 3-mm-thick or larger tissues. We purchased multiple bottles of sodium acrylate, made 38% (w/v) solutions in DI water, and checked their colors. The sodium acrylate bottle exhibiting the least yellow color in the 38% (w/v) solution was used to make the monomer solution. The monomer solution was centrifuged at 7,200g for 15 min at 4 °C and only the supernatant was used. Alternatively, the monomer solution was made without adding VA-044 and then was placed at 4 °C for more than 3 d, and the supernatant was used after adding VA-044. After the monomer solution incubation, the tissue was placed between slide glasses sealed with BluTack (Bostik, Australia) to be immersed in the monomer solution. MAP gel embedding was performed under nitrogen gas purge (10 p.s.i.) at 33 °C for 4 h. Care was taken not to trap any air bubbles inside the tissue and surrounding monomer solution. After gelation, gel formed outside of the tissue was carefully removed and the tissue was rehydrated in PBS for several hours before it was placed into DI water for tissue expansion. The expansion ratio was quantified by comparing tissue thickness before and after expansion.

SHIELD-MAP validation: fluorescence retention. To quantify tissue fluorescence preservation by SHIELD during MAP processing, without being affected by mouse-to-mouse and cell-to-cell fluorescent transgene variability, Thy-1 H+YFP mice littermates were perfused with PFA or SHIELD perfusion solution (N = 3 mice for PFA and N = 4 mice for SHIELD) and the brains were processed according to their respective protocols (see "PFA, CLARITY, GA-SWITCH, PACT and iDISCO+ processing" and "SHIELD whole organ processing protocol"). After postfixation and washing in PBS with 0.02% sodium azide, 200-μm-thick sections were made with a vibratome and their surfaces were imaged to assess the initial YFP fluorescence of selected set of cells in cerebral cortices from two different brain coordinates. Both PFA and SHIELD tissues were subjected to the same delipidation condition (37 °C 5 d, 300 mM SDS solution) and then MAP-processed for expansion. Afterwards, the same set of previously imaged cells was imaged again. Total fluorescence inside the set of cells before and after MAP processing was used to calculate fluorescence retention.

SHIELD-MAP validation: distortion analysis on SHIELD-MAP tissue. To quantify tissue distortion by SHIELD-MAP processing, we used the previously established experimental protocol and algorithm[28]. 200-μm-thick SHIELD mouse brain tissue expressing EGFP was imaged after incubation in Protos-based immersion medium. Special care was taken to mount the sample without any stretching or compression. After unmounting and washing in PBS, the imaged tissue was MAP-processed and then expanded in DI water. The same region of the tissue was imaged again with the same microscope and objective lenses. Neuronal structures expressing EGFP were used as 3D geometrical markers to perform distortion analysis.

Semiautomated spine segmentation was performed on images acquired from the expanded SHIELD-MAP tissue with a 40×, 1.25 NA lens (79 nm × 79 nm pixel size for the expanded sample corresponding to a 26 nm × 26 nm pixel size for the pre-expansion sample) or a 20×, 1.0 NA lens (63 nm × 63 nm pixel size postexpansion corresponding to 21 nm × 21 nm pixel size pre-expansion) using Imaris software (Bitplane).

Integrated circuit mapping. PV-Cre mice (Jackson ImmunoResearch Laboratories, stock number 008069) and AAV-FLEX-mRuby2-Synaptophysin-EGFP injection were used to target PV$^+$ neurons in the right hemisphere globus pallidus externa (GPe; −0.15 mm, +2.1 mm and +3.4 mm in the AP, ML and DV axes). Three weeks after virus injection, brains were SHIELD-processed. After the SHIELD-ON step, the brains were washed in PBST

and then sectioned to make a 1-mm-thick sagittal block harboring most of the GPe, subthalamic nucleus (STN) and substantia nigra reticulata (SNr) (1.04 mm–2.04 mm in the ML axis from the bregma).

After clearing, the tissue block was stained with FISH probes targeting *Gad1* as described above in the FISH experimental section. Hybridization was conducted for 2 d at 37 °C followed by stringent washing with 2× SSCT, 50% (v/v) formamide for 1 h at RT three times each, 2× SSCT, 30% (v/v) formamide overnight at RT, and 2× SSCT at RT for 1 h three times each. HCR was performed for 2 d using the B1-Cy5 hairpin at 240 nM, and washing was performed for 1 d using 2× SSCT. All samples were imaged after incubation in Protos-based immersion medium at RT. The part of the tissue block including GPe, STN, nRT, GPi and SNr was imaged using a confocal microscope. *Gad1* FISH HCR signal was destained by DNase I treatment (4716728001, Roche, Switzerland; 20:2,000 in PBS at RT for 12 h). The sample was then stained with rabbit anti-calretinin antibody (ab702, Abcam, MA) for several days and imaged using the confocal microscope. The tissue was further MAP-processed for super-resolution imaging. After the threefold linear expansion in DI water, a light-sheet microscope (SmartSPIM, Lifecanvas Technologies, MA) with a 10×, 0.6 NA objective were used to image the expanded sample.

A total of three 3D datasets were generated from the same sample. Confocal imaging of the tissue after *Gad1* mRNA FISH resulted in a 7.3-GB Imaris file. Subsequent confocal imaging in the tissue after calretinin immunostaining generated a 6-GB Imaris file. Light-sheet microscope imaging of the SHIELD-MAP expanded tissue resulted in 2.1 TB of tiff files, which were 2× downsampled and then were stitched to produce a 158-GB Imaris file. The latter Imaris file was used to reconstruct axon arborization of a single GPe-PV+ neuron with its putative axosomatic connections in multiple brain areas. Processing of the 3D images was done on a PC with Intel i7 3.4-GHz processor, 128 GB RAM and a graphics card with 4 GB memory.

Axon tracing was conducted via rigorous review of the volumetric data using Imaris software (Bitplane). A PV-mRuby+ neuron was chosen and its axon was traced semiautomatically with the help of Imaris software's filament tracer (using its 'autodepth' or 'manual' mode). Tracing accuracy was continuously assessed by examining the data from multiple angles of view and multiple optical planes. In the event of any ambiguity, raw image volumes were used to confirm the accuracy of axonal tracing. For especially dense areas that needed even further confirmation (for example, axon ramification near target neuronal soma), the tissue area in question was imaged via a confocal microscope with a 25×, 0.95 NA objective lens after full tissue expansion. The entire trace of the neuron was confirmed by at least two individuals. The confocal microscope and the 25×, 0.95 NA objective were used to image areas with putative axosomatic connectivity. The pre-expansion voxel size was 30 nm in the *x* and *y* axes and 0.333 μm in the *z* axis.

The confocal image volumes for regions of interest were used to resolve axon ramification and Syp-EGFP+ presynaptic boutons in the putative axosomatic connections of downstream neurons.

To count *Gad1*+ Syp-EGFP+ neurons in the SNr of this sample, multiple optical sections with a fixed interval (100 μm) were unbiasedly selected from the image volume and then all neurons in the SNr area were counted. mRuby2+ neurons were counted from the entire volume of GPe.

Attenuation coefficient. Light attenuation by PFA and P3PE-processed samples were quantified with a method based on a previous publication[70]. Briefly, 100-μm-thick PFA- and P3PE-processed tissue sections were imaged with a transmitted fluorescence light microscope (EVOS FL, ThermoFisher). The intensity of transmitted light through the samples was measured by calculating the mean intensity of the part of the image containing cerebral cortical layers 2–5 to calculate the attenuation coefficient based on the Beer–Lambert law:

$$I = I_0 \times e^{-\mu \times L}$$

where I is the intensity of the light transmitted through the sample, I_0 is the light reached the detector without sample on its light path, μ is attenuation coefficient and L is the thickness of the sample.

Refractive index measurement. PFA-fixed human brain tissue stored in PBS with 0.02% sodium azide was cut in two, and one half was P3PE-fixed by incubating in the supernatant of 10% (w/v) P3PE in PBS at 4 °C for 24 h and then in pH 10, 0.1 M carbonate buffer at 37 °C for 24 h. After washing in PBS with 0.02% sodium azide, the PFA-fixed half and further P3PE-fixed half were completely dried and their refractive indices at 437.2 nm, 487.7 nm and 589.3 nm were measured with a refractometer (Abbermat WR-MW, Anton Paar, Austria).

Statistics and reproducibility. All statistical tests were performed in Graphpad Prism 6. *n* values, type of replicate and results of the statistical tests are indicated in main text or figure legends. Here is the information on the reproducibility of representative results shown in figures and supplementary figures. In **Figure 1**, data in **j,k,m** were repeated two more times with similar results, and data in **l** were repeated one time with a similar result. In **Figure 2**, experiments in **a–c, i** and **m** were repeated 3 times independently to make the graphs in **d, j** and **n**, respectively. Data in **f** and **g** were confirmed in 2 independent experiments with similar results. The experiment for **k** and **l** was done once. Data in **o** and **p-q** were reproduced in 2 and 3 independent experiments, respectively, with similar results. In **Figure 3**, data in **a,b** and in **e** were confirmed in 4 and 3 independent experiments, respectively, to produce the bar graphs in **c,d** and **f**, respectively. Results in **g** were confirmed in 7 independent experiments with similar results. In **Figure 4**, results in **d–f** were confirmed at least in 2 independent experiments with similar results. Experiments in **g–i** were repeated 3 times with similar results. Experiments in **a–c** were done once. In **Figure 5**, experiments in **b–d, f, j** and **m,n** were repeated in 3, 10, 2 and 2 independent trials with similar results. Experiments in **e,j** were done twice in total with similar results. Experiments in **o** were done once. The results in **h** were repeated in 4 different independent experiments to make graph in **i**. In **Figure 6**, experiments in **b,c,e** were repeated independently 4 times with similar result. Experiments in **g–i** were repeated in 10 other cells with similar results. In **Supplementary Figure 1**, experiments in **b–e** were repeated independently 2 times with similar results. In **Supplementary Figure 2**, experiments in **e** were done at least in 2 independent experimental trials and provided similar results. The experiment in **d** was done once. The results in **f** and **g** were obtained in 3 and 4 independent experiments, respectively, to generate bar graphs in **Figure 2j** and **Supplementary Figure 2h**, respectively. In **Supplementary Figure 3**, experiments in **a–c, d, e** and **f–h** were done in 10, 3, 10 and 3 independent trials, respectively, with similar results. Experiments in **j** were repeated 3 times independently to make the bar graph in **i**. In **Supplementary Figure 4**, data in **a,b** were confirmed at least in one more of independent experiment with similar results. In **Supplementary Figure 5**, data in **c** were confirmed in more than 10 independent experiments with similar result. Experiments in **d** were repeated three times with similar results. The experiment in **e** was done once.

Code availability. The custom code used in this study is available from the corresponding author upon reasonable request.

Reporting Summary. Further information on research design is available in the **Nature Research Reporting Summary** linked to this article.

Data availability. The data supporting the findings of this study are available from the corresponding author upon reasonable request.

56. Halgren, T.A. Merck molecular force field. I. Basis, form, scope, parameterization, and performance of MMFF94. *J. Comput. Chem.* **17**, 490–519 (1996).
57. Halgren, T.A. Merck molecular force field. II. MMFF94 van der Waals and electrostatic parameters for intermolecular interactions. *J. Comput. Chem.* **17**, 520–552 (1996).
58. Arpino, J.A.J., Rizkallah, P.J. & Jones, D.D. Crystal structure of enhanced green fluorescent protein to 1.35 Å resolution reveals alternative conformations for Glu222. *PLoS One* **7**, e47132 (2012).
59. Ryckaert, J.-P., Ciccotti, G. & Berendsen, H.J.C. Numerical integration of the cartesian equations of motion of a system with constraints: molecular dynamics of n-alkanes. *J. Comput. Phys.* **23**, 327–341 (1977).
60. Yang, B. *et al.* Single-cell phenotyping within transparent intact tissue through whole-body clearing. *Cell* **158**, 945–958 (2014).
61. Renier, N. *et al.* Mapping of brain activity by automated volume analysis of immediate early genes. *Cell* **165**, 1789–1802 (2016).
62. Choi, H.M.T., Beck, V.A. & Pierce, N.A. Next-generation in situ hybridization chain reaction: higher gain, lower cost, greater durability. *ACS Nano* **8**, 4284–4294 (2014).

63. Chen, F. *et al.* Nanoscale imaging of RNA with expansion microscopy. *Nat. Methods* **13**, 679–684 (2016).

64. Shah, S. *et al.* Single-molecule RNA detection at depth by hybridization chain reaction and tissue hydrogel embedding and clearing. *Development* **143**, 2862–2867 (2016).

65. Moffitt, J.R. & Zhuang, X. RNA imaging with multiplexed error-robust fluorescence in situ hybridization (MERFISH). *Methods Enzymol.* **572**, 1–49 (2016).

66. Dean, K.M., Roudot, P., Welf, E.S., Danuser, G. & Fiolka, R. Deconvolution-free subcellular imaging with axially swept light sheet microscopy. *Biophys. J.* **108**, 2807–2815 (2015).

67. Hedde, P.N. & Gratton, E. Selective plane illumination microscopy with a light sheet of uniform thickness formed by an electrically tunable lens. *Microsc. Res. Tech.* **6**, 2181 (2016).

68. Oh, S.W. *et al.* A mesoscale connectome of the mouse brain. *Nature* **508**, 207–214 (2014).

69. Schnell, S.A., Staines, W.A. & Wessendorf, M.W. Reduction of lipofuscin-like autofluorescence in fluorescently labeled tissue. *J. Histochem. Cytochem.* **47**, 719–730 (1999).

70. Gómez-Gaviro, M.V. *et al.* Optimized CUBIC protocol for three-dimensional imaging of chicken embryos at single-cell resolution. *Development* **144**, 2092–2097 (2017).

nature research

Corresponding author(s):

Reporting Summary

Nature Research wishes to improve the reproducibility of the work that we publish. This form provides structure for consistency and transparency in reporting. For further information on Nature Research policies, see Authors & Referees and the Editorial Policy Checklist.

Statistical parameters

When statistical analyses are reported, confirm that the following items are present in the relevant location (e.g. figure legend, table legend, main text, or Methods section).

n/a	Confirmed	
☐	☒	The exact sample size (*n*) for each experimental group/condition, given as a discrete number and unit of measurement
☐	☒	An indication of whether measurements were taken from distinct samples or whether the same sample was measured repeatedly
☐	☒	The statistical test(s) used AND whether they are one- or two-sided *Only common tests should be described solely by name; describe more complex techniques in the Methods section.*
☐	☒	A description of all covariates tested
☐	☒	A description of any assumptions or corrections, such as tests of normality and adjustment for multiple comparisons
☐	☒	A full description of the statistics including central tendency (e.g. means) or other basic estimates (e.g. regression coefficient) AND variation (e.g. standard deviation) or associated estimates of uncertainty (e.g. confidence intervals)
☐	☒	For null hypothesis testing, the test statistic (e.g. F, t, r) with confidence intervals, effect sizes, degrees of freedom and P value noted *Give P values as exact values whenever suitable.*
☒	☐	For Bayesian analysis, information on the choice of priors and Markov chain Monte Carlo settings
☒	☐	For hierarchical and complex designs, identification of the appropriate level for tests and full reporting of outcomes
☒	☐	Estimates of effect sizes (e.g. Cohen's *d*, Pearson's *r*), indicating how they were calculated
☐	☒	Clearly defined error bars *State explicitly what error bars represent (e.g. SD, SE, CI)*

Our web collection on statistics for biologists may be useful.

Software and code

Policy information about availability of computer code

Data collection	Oligo array 2.1 (designing RNA FISH probe), Fluoview (Olympus FV1000 confocal microscope), Leica LAS X (Image acquisition software for Leica confocal microscope SP8), LabView (SmartSPIM image acquisition)
Data analysis	Imaris 5.0, ImageJ, img2curve.m (curvature analysis

For manuscripts utilizing custom algorithms or software that are central to the research but not yet described in published literature, software must be made available to editors/reviewers upon request. We strongly encourage code deposition in a community repository (e.g. GitHub). See the Nature Research guidelines for submitting code & software for further information.

Data

Policy information about availability of data

All manuscripts must include a data availability statement. This statement should provide the following information, where applicable:
- Accession codes, unique identifiers, or web links for publicly available datasets
- A list of figures that have associated raw data
- A description of any restrictions on data availability

The data supporting the findings of this study are available from the corresponding author upon request.

Field-specific reporting

Please select the best fit for your research. If you are not sure, read the appropriate sections before making your selection.

☒ Life sciences   ☐ Behavioural & social sciences   ☐ Ecological, evolutionary & environmental sciences

For a reference copy of the document with all sections, see nature.com/authors/policies/ReportingSummary-flat.pdf

Life sciences study design

All studies must disclose on these points even when the disclosure is negative.

Sample size	No statistical methods were used to predetermine sample size.
Data exclusions	No data were excluded from analysis.
Replication	Preservation of Fluorescence protein, endogenous protein, mRNA transcript of SHIELD tissue, and tissue architecture preservation/ deformation property of SHIELD have been replicated in multiple other projects that SHIELD tissue has been used and currently running in our lab with/without collaboration with other labs.
Randomization	In all the experiments, mice, tissue, or GFP/BSA samples were randomly assigned to each experimental group. Whenever it is possible, the effect of treatments were assessed by comparing before and after treatment within the same tissue.
Blinding	Blinding wasn't employed for our study excluding Fig 6's tracing results which have been confirmed at least by two individuals with blinding.

Reporting for specific materials, systems and methods

Materials & experimental systems

n/a	Involved in the study
☒	Unique biological materials
☐	☒ Antibodies
☒	Eukaryotic cell lines
☒	Palaeontology
☐	☒ Animals and other organisms
☒	Human research participants

Methods

n/a	Involved in the study
☒	ChIP-seq
☒	Flow cytometry
☒	MRI-based neuroimaging

Antibodies

Antibodies used	Antigen,Vendor,Catalog #,Host species,Clonality,Dilution Calbindin,Abcam,ab11426,Rabbit,P,1 to 200 Calbindin,Abcam,ab82812,Mouse,M,1 to 200 Calbindin,SWANT,300,Mouse,M,1 to 200 Calretinin,Abcam,ab702,Rabbit,P,1 to 200 Calretinin,SWANT,6B3,Mouse,M,1 to 200 Calretinin,SWANT,CG1,Goat,P,1 to 200 Calretinin,SWANT,7697,Rabbit,P,1 to 200 Choline Acetyltransferase(ChAT),Millipore,AB144P,Goat,P,1 to 200 GABA,Sigma,A2052,Rabbit,P,1 to 200 GABA,Abcam,ab17413,Guinea Pig,P,1 to 200 GFAP,Abcam,ab48050,Rabbit,P,1 to 200 GFAP,BioLegend,835301,Mouse,M,1 to 200 GFAP,Aves,GFAP,Chicken,P,1 to 200 GFAP,CST,3670S,Mouse,M,1 to 200 Iba1,Wako,019-19741,Rabbit,P,1 to 200 NeuN,BioLegend,834501,Mouse,M,1 to 200 NeuN,CST,12943S,Rabbit,M,1 to 200 NeuN,CST,24307S,Rabbit,M,1 to 200 NeuN,Millipore,MAB377,Mouse,M,1 to 200 Neuropeptide Y,CST,11976S,Rabbit,M,1 to 200 Parvalbumin,Abcam,ab11427,Rabbit,P,1 to 200

```
Parvalbumin,Abcam,ab32895,Goat,P,1 to 200
Parvalbumin,Thermo,PA1-933,Rabbit,P,1 to 200
Parvalbumin,SWANT,PV27,Rabbit,P,1 to 200
Somatostatin,Immunostar,20067,Rabbit,P,1 to 200
Somatostatin,Abcam,ab30788,Rat,M,1 to 200
Tryptophan hydroxylase 2,Thermo,PA1-778,Rabbit,P,1 to 200
Tyrosine hydroxylase,Biolegend,818001,Mouse,M,1 to 200
Tyrosine hydroxylase,Aves,TYH,Chicken,P,1 to 200
Tyrosine hydroxylase,Abcam,ab112,Rabbit,P,1 to 200
SATB2,Abcam,ab92446,Rabbit,M,1 to 200
TBR1,Abcam,ab31940,Rabbit,P,1 to 200
Neurofilament-M,Aves,NFM,Chicken,P,1 to 200
Neurofilament-H,CST,2836S,Mouse,M,1 to 200
Neurofilament-L,CST,2835S,Mouse,M,1 to 200
SMI-32,BioLegend,801701,Mouse,M,1 to 200
MAP2,CST,8707S,Rabbit,M,1 to 200
Myelin Basic Protein,Abcam,ab134018,Chicken,P,1 to 200
Myelin Basic Protein,Abcam,ab7349,Rat,M,1 to 200
SMI-312,Biolegend,837904,Mouse,M,1 to 200
FoxP2,Abcam,ab1307,Goat,P,1 to 200
FoxP2,Abcam,ab16046,Rabbit,P,1 to 200
cFos,Santa Cruz,SC-52,Rabbit,P,1 to 200
cFos,CST,2250S,Rabbit,M,1 to 200
GAD67,Abcam,ab75712,Chicken,P,1 to 200
Histone H3 (Alexa 647-conjugated),CST,12230S,Rabbit,M,1 to 200
GFP,Thermo,A11122,Rabbit,P,1 to 200
GFP (Alexa 488 conjugated),Thermo,A21311,Rabbit,P,1 to 200
GFP (Alexa 555 conjugated),Thermo,A31851,Rabbit,P,1 to 200
GFP (Alexa 594 conjugated),Thermo,A21312,Rabbit,P,1 to 200
GFP (Alexa 647 conjugated),Thermo,A31852,Rabbit,P,1 to 200
RFP,Rockland,600-401-379,Rabbit,P,1 to 200
RFP-CF660R,Biotium,20478,Rabbit,P,1 to 200
```

Validation | Antibody validation has been done by 1) comparing antibody signals to established scientific articles that performed immunostaining for the same targets, 2) comparing the distribution of the positive cells to Allen brain ISH data.

Animals and other organisms

Policy information about studies involving animals; ARRIVE guidelines recommended for reporting animal research

Laboratory animals | Male or female young adult (2-4 month, median age : 3 month) C57BL/6 mice(species : Mus Musculus) were used.

Wild animals | N/A

Field-collected samples | N/A